



TALLINN UNIVERSITY OF TECHNOLOGY
SCHOOL OF ENGINEERING
Department of Materials and Environmental Technology

**STUDY ON THE PHOTOCATALYTIC ACTIVITY OF
HYDROTHERMALLY GROWN ZnO NANORODS ON
THE DEGRADATION OF DIFFERENT DYE
POLLUTANTS**

**H ÜDROTERMAALSET KASVATUD ZnO NANOVARRASTE
FOTOKATALÜÜTILISE VÕIMEKUSE UURING ERINEVATE
VÄRVSAASTEAINETE LAGUNDAMISEL**

MASTER THESIS

Üliõpilane: Chukwu Richard

Üliõpilaskood: 184643KAYM

Juhendaja: Dr. Tatjana Dedova

Tallinn 2020

AUTHOR'S DECLARATION

Hereby I declare, that I have written this thesis independently.

No academic degree has been applied for based on this material. All works, major viewpoints and data of the other authors used in this thesis have been referenced.

"20"05..... 2020.....

Author:

/signature /

Thesis is in accordance with terms and requirements

"....." 20....

Supervisor:

/signature/

Accepted for defence

"....."20... .

Chairman of theses defence commission:

/name and signature/

Non-exclusive Licence for Publication and Reproduction of Graduation Thesis¹

I, Chukwu Richard (name of the author) (date of birth: 03.02.1985) hereby
1. grant Tallinn University of Technology (TalTech) a non-exclusive license for my thesis:

Study on the photocatalytic activity of hydrothermally grown ZnO nanorods on the degradation of different dye pollutants.

(title of the graduation thesis)

supervised by Dr. Tatjana Dedova

(Supervisor's name)

1.1 reproduced for the purposes of preservation and electronic publication, incl. to be entered in the digital collection of TalTech library until expiry of the term of copyright;

1.2 published via the web of TalTech, incl. to be entered in the digital collection of TalTech library until expiry of the term of copyright.

1.3 I am aware that the author also retains the rights specified in clause 1 of this license.

2. I confirm that granting the non-exclusive license does not infringe third persons' intellectual property rights, the rights arising from the Personal Data Protection Act or rights arising from other legislation.

¹ *Non-exclusive Licence for Publication and Reproduction of Graduation Thesis is not valid during the validity period of restriction on access, except the university's right to reproduce the thesis only for preservation purposes.*

_____ *(signature)*

_____ *(date)*

Department of Materials and Environmental Technology

THESIS TASK

Student: Chukwu Richard, 184643KAYM
Study programme, Material and Processes of Sustainable Energetics
main speciality: Processes of Sustainable Energetics
Supervisor(s): Research Scientist, Dr. Tatjana Dedova, 620 3369

Thesis topic:

(in English): Study on the photocatalytic activity of hydrothermally grown ZnO nanorods on the degradation of different dye pollutants

(in Estonian): Hüdrotërmaalselt kasvatatud ZnO nanovarraste fotokatalüütilise võimekuse uuring erinevate värvsaasteainete lagundamisel

Thesis main objectives:

1. To synthesize ZnO nanorods via hydrothermal growth.
2. To study the morphological, structural, optical characteristic of the as synthesized nanorods.
3. To study the photocatalytic properties of the as synthesized nanorods using three different organic dye pollutants while keeping the dye concentration, and other parameters constant.

Thesis tasks and time schedule:

No	Task description	Deadline
1.	Study of basic research methods	1st sem
2.	Literature review	2nd sem 3rd sem
3.	Experimental section	4th sem

Language: **Deadline for submission of thesis:** ".....".....201....a

Student: ".....".....201....a
/signature/

Supervisor: ".....".....201....a
/signature/

Consultant: ".....".....201....a
/signature/

Head of study programme: ".....".....201.a
/signature/

TABLE OF CONTENTS

TABLE OF CONTENTS	5
PREFACE	7
LIST OF ABBREVIATION AND SYMBOLS	8
INTRODUCTION.....	9
1. LITERATURE REVIEW	11
1.1 Water Pollution problem	11
1.1.1 Dyes.....	13
1.2 Introduction to water treatment technologies: Advanced oxidation processes. 14	
1.3 Photocatalysis	16
1.3.1 Photocatalytic mechanism	16
1.3.2 Factors affecting photocatalytic activity	18
1.3.3 Size, structure and phase composition of semiconductor material.....	18
1.3.4 Light intensity.....	19
1.3.5 Temperature.....	19
1.3.6 Presence of inorganic ions	19
1.3.7 Oxygen vacancies	20
1.3.8 Calcination Temperature:	21
1.3.9 Concentration of the pollutant.....	21
1.3.10 Photocatalyst Loading	22
1.3.11 Effect of pH of the solution	23
1.4 Characterization methods.....	24
1.4.1 X – ray diffraction	24
1.4.2 Scanning electron microscopy (SEM)	25
1.4.3 Photoluminescence (PL)	26
1.4.4 X- ray photoelectron spectroscopy (XPS).....	27
1.4.5 UV – Vis spectroscopy.....	28
1.5 ZnO properties.....	30

1.6	ZnO structure	31
1.7	Nanostructured ZnO	32
1.8	Applications of ZnO	32
1.9	ZnO by hydrothermal growth	33
1.10	Literature overview on ZnO rodlike crystals grown by hydrothermal method	34
1.10.1	Influence of precursor on ZnO crystals morphology (chemical composition, concentration and pH)	35
1.10.2	Influence of synthesis time on the hydrothermal growth of ZnO crystals	36
1.10.3	Influence of hydrothermal temperature on the morphology of ZnO crystals	37
1.10.4	Influence of a seed layer	38
1.11	Summary of literature review.....	39
1.11.1	Aims of the study	41
2.	EXPERIMENTAL PART	42
2.1	Materials and methods for samples preparation.....	42
2.2	Characterization	44
3.	RESULTS AND DISCUSSION.....	46
3.1	SEM Study: Morphology and dimensions of the ZnO layers	46
3.2	XRD study. Structure and phase composition of ZnO layers	46
3.3	UV-VIS Optical Properties	48
3.4	Surface properties of ZnO layers	49
3.5	Photocatalytic activity of the ZnOR photocatalysts	51
3.6	Discussion	53
4.	CONCLUSIONS	56
	SUMMARY	57
	ACKNOWLEDGEMENTS	58
	LIST OF FIGURES	59
	LIST OF TABLES	61
	REFERENCES.....	62

PREFACE

The topic of the following thesis was proposed by Dr. Tatjana Dedova and the work was carried out in the Laboratory of Thin Film Chemical Technologies at the department of Materials and Environmental Technology. Assistance in experimental set up was provided by Dr. Atanas Katerski.

The research aims to study the photocatalytic degradation of three organic dye pollutants namely, methyl orange, methylene blue, and Rhodamine B. The ZnO nanorodlike crystals were synthesized using a precursor solution containing equimolar concentrations (0.01 mol/L) of zinc nitrate hexahydrate ($\text{Zn}(\text{NO}_3)_2 \cdot 6\text{H}_2\text{O}$) and hexamethylenetetramine ($\text{CH}_2)_6\text{N}_4$; HMTA. Processing temperature and time were 120°C and 2 hours, respectively. Growing ZnO_R layers vertical orientation to the substrate was achieved by means of ZnO seed layers deposited by spray pyrolysis onto glass substrates before the hydrothermal procedure.

The ZnO_R were characterized using standard nanomaterial characterization methods. According to XPS and PL study, the relative intensity of OH/Me-O groups for ZnO was 0.4. SEM images reveal nanorod layers of length 1 μm and a diameter between 50 – 150 nm. Photocatalytic studies were carried out under UV illumination. The photocatalytic activity of the ZnO_R was found to be higher for MO and RhB with a degradation efficiency of 68% and 67% respectively. Photocatalytic efficiency for MB decomposition was 55%. Hydrothermal synthesis remains a facile growth approach and has a distinct advantage of scalability for the synthesis of ZnO nanorods, a promising material in the photocatalytic purification of water.

Keywords: ZnO, hydrothermal growth, photocatalysis, dyes, master thesis

LIST OF ABBREVIATION AND SYMBOLS

AOP – Advanced Oxidation Process
BSE - Backscattered electrons
BSE – Back-scattered electrons
CVD - Chemical vapour deposition
EBIC – Electron beam-induced current
ED – Electrolyte deposition
EDX – Energy dispersive X-ray spectroscopy
 E_g - Bandgap energy
GaN – Gallium nitride
HMTA – Hexamethylenetetraamine
MS – Magnetron sputtering
PL - Photoluminescence
PVD - Physical vapour deposition
PZC – Point of zero charge
SE - Secondary electrons
SEM - Scanning electron microscopy
TCO – Transparent conducting oxide
 TiO_2 - Titanium dioxide
USP - Ultrasonic spray pyrolysis
XPS - X-ray photoelectron spectroscopy
XRD - X-ray diffraction
 ZnO_R - Zinc oxide rod(s)
 ZnO_{NR} - Zinc oxide nanorod(s)

INTRODUCTION

The textile industry has created an enormous pollution problem as it is one of the most chemical-intensive industries on earth. The textile industry uses than 8000 chemicals in various processes of textile manufacture, including dyeing and printing. Organic dyes are widely used in leather, textile, pulp and they are dominating pollutants in wastewater [1]. More than 3600 individual textile dyes are being manufactured by the Industry today. During the industrial processing, some of the excess dyes end up as waste and will be discharged as industrial effluent. Annually, more than one million ton of dyes are produced resulting in a discharge of up to 0.28 million tons of wastewater [2]

The light-absorbing nature of these coloured substances mean less light reach aquatic organisms. The colloidal matter present along with colours also increases the turbidity and gives the water a bad appearance and foul smell. Less penetration of sunlight hampers photosynthesis and interferes with the Oxygen transfer mechanism at air water interface. This depletion of dissolved oxygen in water and lessening of the water self-purification process remains the most adverse effect of textile wastewaters. And this poses great danger to marine and human life [3].

It is noteworthy that the majority of dyes are highly toxic especially carcinogenic and mutagenic to human beings. Even at low concentration (<1 mg/L for some dyes), major dyes decrease the transparency of water, consume oxygen and elevate biochemical oxygen demand destroying aquatic life[3]. Therefore, the efficient removal of dyes from industrial effluents poses a significant challenge and necessitates the development of novel water purification methods.

To date, advanced oxidation processes (AOPs) have been studied extensively and seen as a promising technology to clean the toxic dye effluents due to the strong capability to mineralize a wide range of recalcitrant contaminants such as dyes. Some of the advanced oxidation processes include; ozone oxidation, electrochemical oxidation [4], wet oxidation [5], sonocatalysis [6], chemical oxidation, and processes based on the Fenton reagent [7]. The focus on advanced oxidation processes is as a result of their efficiency, wide process operability, absence of secondary wastes and the ability to handle fluctuating flow rates. Among AOPs, a heterogeneous photocatalysis, involving photocatalytic degradation of dyes using semiconductor photocatalyst and light irradiation is considered as an efficient method for dye mineralization and has been chosen for this study.

TiO₂ and ZnO are the most studied and efficient photocatalysts for dye degradation up to now and attractive due to their low cost, low toxicity, earth-abundance, strong

oxidizing nature, and long term photostability [8]. The greatest advantage of ZnO compared to many other metal oxides lies in its wide UV-Vis absorbance spectrum. Hydrothermally grown ZnO nanorods are promising photocatalytic material due to high surface areas, ease of preparation, and the cost-effectiveness of the material. The hydrothermal growth method of the ZnO layers is one of the most popular technique so far. The relevance of the hydrothermal method is also supported by the greater number of publications on the hydrothermal growth of ZnO compared to the publications on other synthesis methods. According to ISI Web of Science [9], the number of publications between 2008-2020 containing the hydrothermal growth of ZnO is ca. 5000 publications. However, most hydrothermally developed nanostructures are loose, are not bound to the substrate structures, which highlights prevailing challenges in the fabrication of c-axis oriented ZnO_R nanorod crystals which are highly crystalline and immobilized onto the glass substrate.

Of all coloured materials emanating from textile industries, azo dyes account for the largest class, making up 60-70% of all organic dyes produced in the world. Methyl orange (MO) is a typically anionic azo type dyeing material which has been extensively used in the printing, food, textile, scientific research, and pharmaceutical industries. Methylene blue (MB) is widely known and used extensively for dyeing silk, cotton and wool [2]. Rhodamine B is a bright pink, fluorescent cationic xanthene dye used which is also used as a textile and food colourant [10]. Therefore, those types of dyes have been chosen for this study.

Although a variety of studies on photocatalytic degradation of dye molecules exist, many of these studies focus either on individual pollutant dye or individual photocatalysts. The parameters on photocatalytic degradation, such as concentration of dye, power of illumination, surface area of the photocatalyst vary from study to study.

To overcome the shortcomings of previous studies, we vary the type of pollutant while keeping all other factors constant.

1. LITERATURE REVIEW

1.1 Water Pollution problem

Water pollution is one of the major problems plaguing many industrialized and developing nations. In fact, the WHO/UNICEF Joint Monitoring Programme for Water Supply and Sanitation estimated that at least 2.2 billion people worldwide lack access to safe drinking water [11]. Every day, 2 million tons of sewage and industrial and agricultural waste are discharged into the world's water (UN WWAP 2003).

The sources of pollution are diverse. The major source is however from city generated sewage which is discharged into surface waters like rivers and lakes. Waste can range from food garbage, scrap metals to oils and solvent. The problem of water pollution has been further compounded by industrialization and urbanization. Waste from manufacturing plants include corrosive and ignitable chemicals. Textile mills account for one-fifth of the world's industrial water pollution, utilizing about 20,000 different chemicals, many of them carcinogens.[12]

According to McKinney and Schoch [13], pollutants can also be categorized by the nature of the activity that produced them. They are either human (body and domestic wastes, household chemical runoff), agricultural (sediment particles, pesticides and nutrients) or industrial (organic chemicals, heavy metals, paints, plastics, pharmaceutical by-products, oils and dyes). Of the three sources, industrial wastes contribute the largest in terms of water pollutions – more than 70% is dumped into surface waters without pre-treatment [14]. This is problematic as industrial wastes such as heavy metals, antibiotics and synthetic organic compounds have the property of being persistent, toxic and in the case of heavy metals, non-degradable.

The World Bank estimates that 17 to 20 percent of industrial water pollution comes from textile dyeing and finishing treatment given to fabric. Some 72 toxic chemicals have been identified in water solely from textile dyeing, 30 of which cannot be removed. This represents an appalling environmental problem for the clothing and textile manufacturers.

Therefore, the study of this thesis represents an approach to clean the water from certain dyes, such as methyl orange (MO), methyl blue (MB) and Rhodamine blue (RhB).

Table 1.1: Classification of water pollutants [28]

Nature of contamination	Source	Concerns
Organic matter	Effluents from various industries and built-up (sewage)	Biological Oxygen Demand (BOD), Dissolved Oxygen (DO)
Pathogens (Microbes)	Sewage and livestock	Fecal coliform (Coliform), <i>Escherichia coli</i> , <i>Shigella</i> and <i>Salmonella</i>
Nutrients	Runoff from agricultural activities and industrial discharge	Total N and P
Salinization	Leached from alkaline soils, over irrigation of saltwater, over pumping coastal aquifers	EC, p H and sodium toxicity.
Heavy metals	Variety of sources viz., industries, mining, agricultural activities and vehicles	Hg, Pb, Cd, Cr, Hg and As
Toxic synthetic organic compounds	MSW, industries, automobiles	PAHs, PCBs, pesticides (lindane, DDT, PCP, Aldrin, Dieldrin, Endrin, Isodrin), dyes (methyl orange,

1.1.1 Dyes

Dyes have long history, dating back to 1856 when W.H. Perkin accidentally synthesized Mauveine, a basic dye. Several other synthetic dyes soon followed. Some include Aniline Blue, Methylene Blue Methyl Orange, Rhodamine B, and Tartrazine. As the textile industry grew and spawned newer synthetic fibre, advances were also made in the development of newer reactive dyestuffs with higher washing fastness. The textile industry's host of dye chemicals constitutes the major pollutants threatening access to safe water. Over 10,000 different types of dyes and pigments are manufactured annually. Meanwhile, for an average mill with a capacity of 60×10^4 m, the amount of effluent discharged is up to 1.5 million liters/day [15].

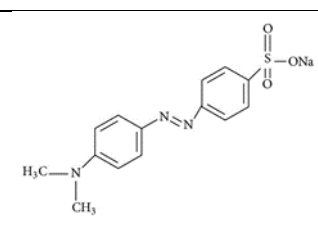
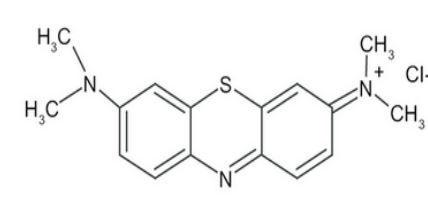
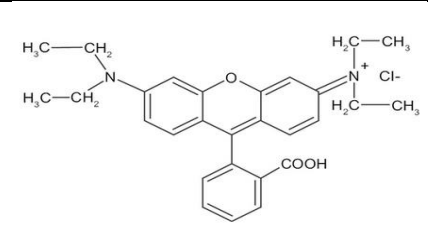
Synthetic dyes can be grouped into several categories: basic or cationic dyes, the direct dyes, the acid dyes, premetallized dyes, sulfur dyes, azoic dyes, vat dyes, and collective dyes. Basic dyes are water-soluble cationic dyes. Electrostatic attractions arise when basic dyes are applied to substrate with an anionic character. Examples of basic dyes include Methylene Blue, Rhodamine B and Methyl Orange [16].

Textile wastewater is peculiar because it contains high colour, and a huge amount of toxic chemicals. Even in low concentration, the colour can constitute aesthetic pollution and block the sunlight from reaching aquatic organisms like planktons which require sunlight for photosynthesis. The physicochemical nature of the wastewater limits the effectiveness of conventional water treatment methods [17].

Methyl orange (MO) is an anionic dye used as pH indicator due to the distinct colour change it undergoes in acidic (red) and basic (yellow) media. It contains the azo functional group in its basic structure $\text{Ar}-\text{N}=\text{N}-\text{Ar}'$, where Ar and Ar' represent aromatic rings and $-\text{N}=\text{N}-$ is the azo functional group. The azo group is a strong chromophore (molecules that absorb specific wavelengths of light) and gives the dye its characteristic colour. Methylene blue (MB) is a photoactive phenothiazine dye with a cationic charge. Also known as methylthioninium chloride, it is a solid, odorless, dark green powder that dissolves in water to give a blue solution [16].

It is widely used in silk dyeing. Methylene blue poses several adverse health problems such as nausea, vomiting, diarrhea, breathing difficulties and eye irritation. It is also hard to degrade by traditional technologies. Rhodamine B, also known as Basic Violet, is a widely used industrial dye. It has a cationic charge and exhibits a moderate wash fastness property. It is the component of stamp pad ink and ballpoint pens. It is highly soluble in water and alcohol. This non-volatile organic dye is also a skin irritant and a mutagen [18].

Table 1.2: Structure and properties of dye molecules

Compound	Structural formula	Charge	Molecular formulae	Lambda max (nm)	Solubility in water
MO		Anionic	$C_{14}H_{14}N_3NaO_3$	464	0.5 g/100 ml (20°C)
MB		Cationic	$C_{16}H_{18}ClN_3S_3$	668	3.55 g/100 ml (20°C)
Rh-B		Cationic	$C_{28}H_{31}N_2O_3Cl$	552	0.8 g/100 ml (20°C)

The major problem is that modern synthetic dyes and chemicals have a higher stability, they are usually hydrophilic, persistent and present in larger amounts in textile waste waters. There is a demand for a cost-effective and reliable technique to eliminate contaminants. A potential solution to this difficult problem is the use of advanced oxidation processes.

1.2 Introduction to water treatment technologies: Advanced oxidation processes

Conventional water treatment methods like filtration, flocculation and coagulation have been used in developing countries for a long time. However, these water treatment processes are no longer sustainable and partially eliminate water pollutants. These methods, including adsorption via granular activated carbon (GAC) bear a huge waste disposal cost and do not completely eliminate toxins from the wastewater [19]. In order to be considered safe for drinking and other domestic purposes, water must meet set quality criteria and standards.

Much of the research in water treatment has, therefore, been focused on advanced oxidation processes (AOPs). This is because advanced oxidation processes can be

synergistically combined with conventional drinking water purification technologies. AOPs include a range of advanced oxidative processes such as ozonation (O₃), Fenton (Fe²⁺/H₂O₂), electrolysis (electrodes with current), sonolysis (ultrasounds), photolysis, photocatalysis (light with catalyst), photo-Fenton (Fenton reaction with light) [20]. Figure 1.1 represents an overview of AOPs. Their effectiveness in the decomposition of synthetic organic matter has also been clearly demonstrated [19].

Semiconductor-based photocatalysis has been studied extensively over the years as it offers the greatest potential for the removal of recalcitrant organic species. This process is nondestructive and makes use of the abundant natural energy from the sun. Furthermore, this process is low cost and some of the catalysts used are abundant in nature like titanium dioxide (TiO₂) and zinc oxide (ZnO).

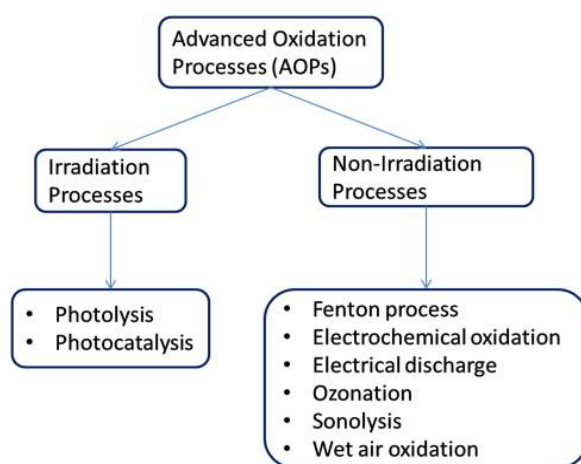


Figure 1.1 Overview of dye removal processes [21]

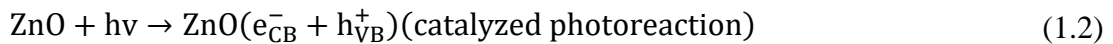
A number of studies and reviews have been undertaken to explore the effectiveness of different photocatalysts in the degradation of Methyl Orange and methylene Blue and Rhodamine B [22][23][24]. The relevance of the ZnO as one of the popular photocatalyst for dyes degradation is approved by large number of publications on dye degradation of ZnO photocatalyst. The number of studies ISI WEB database on this topic is summarized in Table 1.3.

Table 1.3 Number of times ZnO was mentioned in the literature (1980 – 2020) in connection with the degradation of methyl orange, methylene blue, rhodamine-B [9]

Organic Pollutant	Zinc Oxide (ZnO)
Methyl Orange	1,328
Methylene Blue	2,699
Rhodamine B	1,368

1.3 Photocatalysis

In the classic definition, photocatalysis refers to a chemical reaction initiated by the photoabsorption of a catalyst. Homogeneous catalysts are those which exist in the same phase (gas or liquid) as the reactants, while heterogeneous catalysts are not in the same phase as the reactants. Typically, heterogeneous catalysis involves the use of solid catalysts placed in a liquid reaction mixture [25]. The photocatalyst, which is usually a solid material, remains unchanged throughout the process. In photocatalytic reactions, an organic molecule adsorbs on the surface of a semiconductor. Photocatalysis encompasses both photosensitization and catalysed photoreaction. Usually, the organic molecule (for instance, a dye) absorbs light energy and becomes excited.



1.3.1 Photocatalytic mechanism

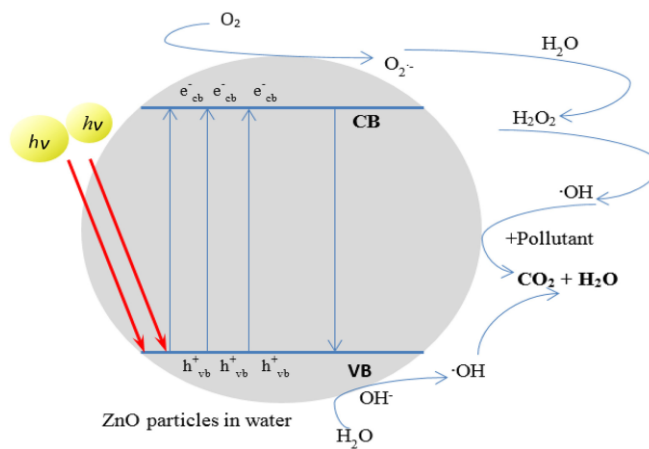


Figure 1.2 The photodegradation of an organic molecule by a ZnO photocatalyst [26]

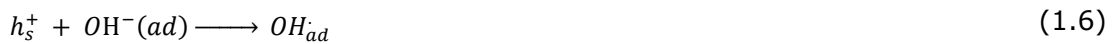
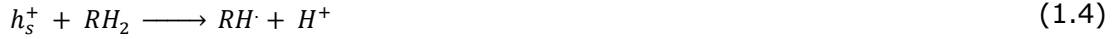
Upon excitation, electrons move from the valence band to the conduction band, and holes migrate to the semiconductor surface where they facilitate a series of oxidation reactions.

Equations 1.3 – 1.15 provide a detailed schematic of the reactions involved in the photocatalytic process.

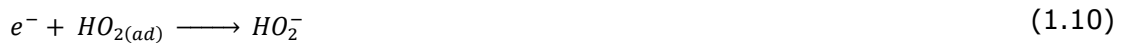
Aqueous solutions contain dissolved oxygen, which acts as the electron acceptor. Oxygen reacts with a trapped electron to form a superoxide radical (equation 1).



The photogenerated holes can react with an organic molecule, water or a surface OH group which is a by-product of the partial hydrolysis of the oxide or the dissociative adsorption of water into protons and the hydroxide ion. The adsorbed hydroxide ions OH_{ad} serve as traps for the holes generated at the surface of the photocatalyst.



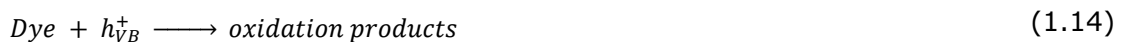
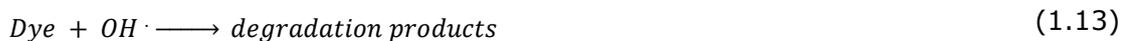
Recombination reactions are also shown in equations 1.7 and 1.8.

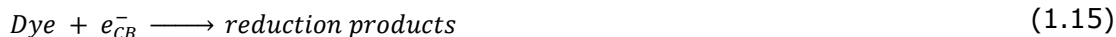


The HO_2^- can combine with a proton to produce hydrogen peroxide which can then be reduced to reactive OH radicals in the solution.



In summary, the dye could be degraded through reactions with radicals, or through direct reaction with electrons and holes.





If the electron transfer rate from the semiconductor to the oxygen is slower than the reaction of holes with the pollutant species or the solvent, it becomes the rate-limiting step in the photocatalytic reaction[27]. If, however, the rate of surface reactions involving the electrons and holes is slower than the rate at which the organic compounds are adsorbed on the surface of the photocatalyst, the surface concentration goes into equilibrium. In this scenario, the rate-limiting step becomes the photo absorption of light [8]. For n-type semiconductors such as ZnO and TiO₂, holes are the limiting active species since there are less photogenerated holes than photogenerated electrons [26].

1.3.2 Factors affecting photocatalytic activity

There are several factors than can impact the photocatalytic process. These factors could be external such as the pH of the solution, temperature, the dye concentration, light intensity and catalyst loading. Other factors are intrinsic to the photocatalyst such as the surface area, crystallinity and morphology of the catalyst.

1.3.3 Size, structure and phase composition of semiconductor material

The structure of semiconductor particles plays a crucial role in the photocatalytic efficiency. For instance, among the common polymorphs of titanium dioxide TiO₂ which include anatase, brookite, rutile and TiO₂ (B), rutile has been identified as the most stable form while the others are metastable[8]. However, the presence of anatase results in a better photocatalytic performance. This is because in the anatase phase, there exists greater hole trapping rates and subsequent lower electron-hole recombination rates, hence, increasing the affinity for adsorption.

It has also been identified that TiO₂ catalysts with mixed-phase exhibits a greater degradation efficiency. This has been ascribed to a synergistic effect between the rutile and anatase phases. The rutile phase, having a smaller bandgap, extends the range of photocatalytic efficiency of TiO₂ into the visible range. The anatase phase offers lower recombination rates. Zinc oxide in the crystal form exists in three phases, the cubic zinc blende, hexagonal wurtzite and the rock salt. The wurtzite phase, which crystallizes at ambient conditions, has been the most commonly used in photocatalytic studies [8].

The particle and agglomerate size of the semiconductor particles is also intrinsically linked to the photodegradation efficiency as there is a direct relationship between the amount of incident photon and the reaction rate. Also, of interest is the influence of the diffusion of target molecules on photocatalysis. One method that has been used to synthesize various nanostructures is the hydrothermal method. ZnO nanorods produced via this method exhibit superior photocatalytic performance. This has been ascribed to the spherical morphology and crystallinity.

1.3.4 Light intensity

Photocatalytic activity is dependent on the amount of light absorbed by a photocatalyst. According to Herrmann [28], the reaction rate was proportional to the radiant flux, ϕ for $\phi < 25 \text{ mW cm}^{-2}$, but varied to square root dependency ($\phi^{0.5}$) when ϕ above 25 mW cm^{-2} . It is suspected that light of a higher intensity results in higher irradiation of the photocatalyst surface and more hydroxyl radicals are produced consequently. However, at higher intensities, the rate of photodegradation becomes independent of the radiant flux and limited only by the mass transfer within the solution. This has been largely attributed to the lack of electron scavengers (O_2), organic molecules within the proximity of the photocatalyst surface or the adsorption of degradation products on the photocatalyst surface [29].

1.3.5 Temperature

Photocatalytic degradation can proceed under ambient conditions of temperature and pressure due to photonic activation which eliminates the need for external heating and makes semiconductor photocatalysis a less energy-intensive process. While the optimum temperature for photocatalysis remains at $20 - 80 \text{ }^\circ\text{C}$, an increase in the reaction temperature may generally increase the reaction rate. However, a higher temperature could also interfere with the adsorptive capacities of the reacting species [28].

1.3.6 Presence of inorganic ions

To obtain a high photocatalytic efficiency, we must take the necessary steps to prevent the recombination of electrons and holes. One possible solution is the addition of inorganic species. Inorganic oxidants improve efficiency either through:

- i. The prevention of electron-hole recombination via electron-trapping.
- ii. Generation of other radicals or oxidizing species.
- iii. Increase in the concentration of hydroxyl radicals.[29]

Favourable inorganic oxidants include H_2O_2 , $S_2O_8^{2-}$, BrO_3^- , SO_3^- . BrO_3^- is a beneficial specie as its decomposition products BrO_2^- and $HOBr$ reduces the recombination rate of electron-hole pairs.

On the other hand, when inorganic ions such as zinc, magnesium, copper, bicarbonate, phosphate, nitrate, sulphate and chloride are present in wastewater, they can heavily impact on the photocatalytic degradation of organic pollutant. These ions lower with the colloidal stability, increase the mass transfer and consequently decrease the surface contact between the photocatalyst and the organic molecule. Nitrates, chlorides and carbonates have also been shown to dampen the surface reactivity of the photocatalyst. It has been postulated that the chloride ions act as hydroxide radical scavengers as shown below,



This results in a reduction in the amount of OH^\cdot present at the photocatalyst surface. Also, it has been reported that $NaOH$, KOH , and $NaHCO_3$ result cause fouling of the photocatalyst. These studies warrant a better understanding as they do not really mirror the real world where a mix of these ions exists and complex reactions occur among them [30][31].

1.3.7 Oxygen vacancies

The electron which reacts with oxygen has been shown to be the electron trapped at or very close to the surface of the semiconductor [27]. The logical explanation is that the trapping of electrons in sites different from where holes are trapped limits the likelihood of recombination and thus result in an increase in the number of electrons available to react with the oxygen. Since the electron trapping sites are localized on the surface, it is more probable that the electron trapping oxygen vacancies are also located on the surface, since they are more easily formed at such locations [27].

1.3.8 Calcination Temperature

Xiaoqing Chen, Zhansheng et al. [32] studied the effect of calcination temperature on the photocatalytic efficiency of ZnO nanorods prepared using the sol-gel method. They compared the photocatalytic activity at different calcination temperatures (300°C, 400°C, 500°C, 600°C) and found that the photocatalyst efficiency increased and then decreased with increasing temperature, as shown in Figure 1.3. This was attributed to the increase in the average particle size from 22.56 to 50.51 nm. ZnO calcined at 400°C had a smaller size and thus more active sites which promote the formation of radicals and provide adsorption sites for the dye molecule.

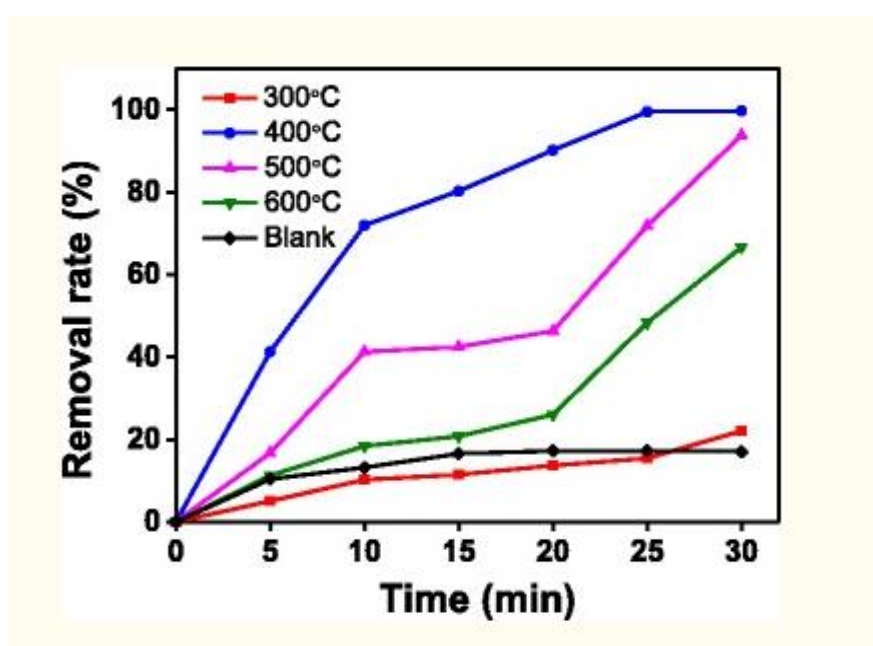


Figure 1.3 Effect of calcination temperature on the photocatalytic properties of ZnO [32]

1.3.9 Concentration of the pollutant

There is a large body of work considering the effect of pollutant concentration on the efficiency of the catalytic process. [33][34][35]. Sayed M Saleh [34] varied the initial concentration of methylene blue between 20 mg/L to 120 mg/L and allowed contact of the photocatalyst with the pollutant for 70 mins. The degradation of MB was found to be significantly affected an increase in the dye concentration as is evident in Figure 1.4. A higher concentration of dye pollutant causes a lowering of the degradation activity of the photocatalyst. As the concentration of the organic pollutant increases, adsorption is increased on the catalyst surface. Consequently, there is an increase in demand for oxidizing radical species. Furthermore, as the concentration of the dye increases, turbidity is enhanced, photons are intercepted and competitive consumption for

generated hydroxyl radical increases. This results in a lowering of photocatalytic activity [29].

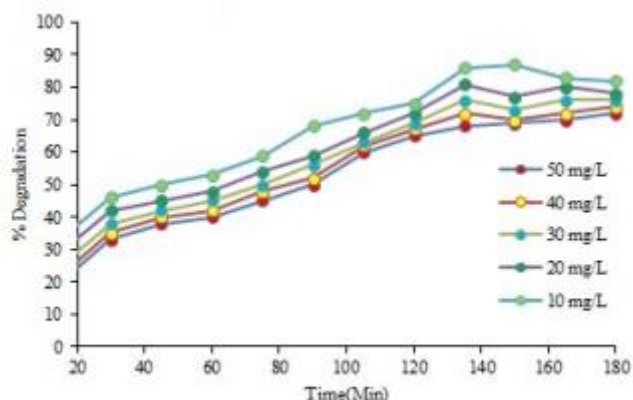


Figure 1.4 Effect of initial dye concentration on the photocatalytic degradation [34]

1.3.10 Photocatalyst Loading

Sayed M Saleh [34] studied the influence of ZnO nanorods load on the photocatalytic degradation of methylene blue in dark and UV – illuminated conditions. The loading of the photocatalyst was between 25 mg/L to 150 mg/L while the exposure time was kept at 70 min. The results of this experiment are shown in Figure 1.5.

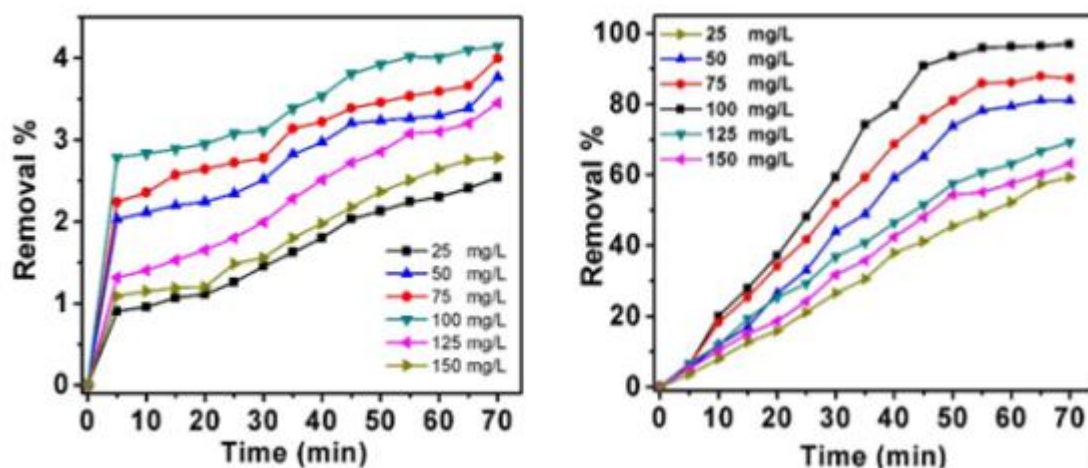


Figure 1.5 Plots showing the removal percent as a function of MB degradation versus Time (min). (a) in the dark; (b) under UV illumination [34]

Xiaoqing Chen, Zhansheng et al. [32] also studied the decomposition of methyl orange, Congo red and direct black in the presence of different concentrations (0.1-0.8 g/L) of ZnO. In both cases, the efficiency increases up to a certain optimal concentration of the

photocatalyst and then decreases with the increment of the photocatalyst amount. This increase in efficiency is due to an increase in the number of reaction sites on the photocatalyst surface. As the number of active sites increase, there is usually an accompanying increase in the number of hydroxyl and superoxide radicals. However, at higher concentrations of the photocatalyst, a blocking effect occurs. The blocking effect is due to the agglomeration of the nanomaterials. This agglomeration enhances turbidity of the solution and prevents the photons from reaching the surface of the nanorods.

1.3.11 Effect of pH of the solution

pH has been found to be one of the most influencing factors affecting photocatalytic activity [29]. This is attributed to the controlling effect it has on the degradation reaction. The pH of the solution affects the surface charge of the catalyst particles and influences the position of conduction and valence bands within a semiconductor. If the pH is lower than the p_{Hpzc} (point of zero charge), the catalyst surface is positively charged but when the pH becomes higher than the p_{Hpzc}, the surface is negatively charged. In low pH solutions, photogenerated holes (h⁺) are considered to predominate while hydroxyl radicals are the major oxidizing species in neutral (pH < pK_a) and alkaline solutions. A number of studies have also shown that as the pH further increases, hydroxyl ions proliferate and are rapidly scavenged thus leading to a reduction in overall photocatalytic efficiency [36].

K. A. Isai and V. S. Shrivastava [37] conducted photocatalytic studies on the degradation of MB dye in the range of pH 1 – 10 using ZnO and Fe-ZnO synthesized via sol-gel method. They found that the percentage of dye removal increased with increasing pH as shown in Figure 1.6, reaching a maximum value in the acidic pH-range. This they attributed to protonation of the catalyst surface which made the surface positively charged so that the dye cations were electrostatically attracted towards the catalyst surface where they eventually become oxidized by the holes on the surface of the catalyst.

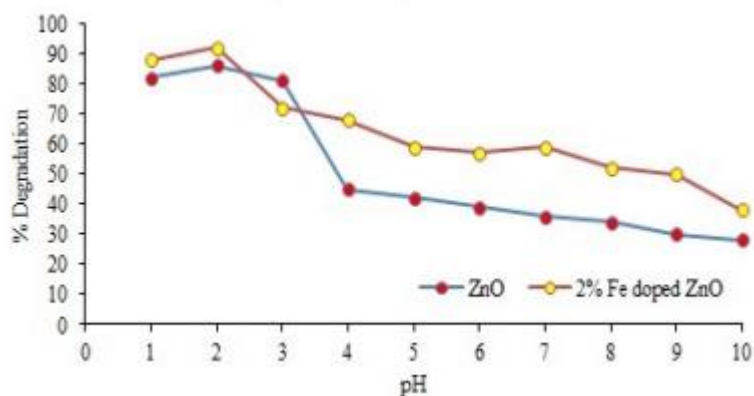


Figure 1.6 Effect of pH on photocatalytic degradation of MB dye under conditions, pH= 1-10. [37]

1.4 Characterization methods

In order to study the properties of photocatalysts, certain techniques have to be employed. The following describes the main techniques utilized in this study.

1.4.1 X-ray diffraction

The X-ray diffraction (XRD) technique is a widely used method used for the in situ and ex situ characterization of nanomaterials and other substances. Methods based on X-ray diffraction by crystals have evolved since 1985 when X-rays were first discovered by Wilhelm Conrad Roentgen. X-rays are photons with energy $\sim 125 \text{ eV} - 125 \text{ keV}$ (wavelength $\lambda \sim 0.01 - 10 \text{ nm}$). [38]

In an X-ray diffraction experiment, a sample is placed within an instrument and illuminated with an incident beam of X-rays. The x-ray tube and detector move in a synchronized manner. The X-rays incident on the material can be elastically (Thompson scattering) or inelastically (Compton scattering) scattered by electrons. In the case of elastic scattering, the energy of the incident photon is equal to that of the scattered photon, and this is responsible for the diffraction process. Inelastic scattering, on the other hand, results in an emitted photon with a lower energy than the incoming photon. The signal from the sample, amplified by the constructive interference of the outgoing radiation, as illustrated in Figure 1.7, is recorded and graphed. The peaks observed in the resulting graph relate to the structure of the sample. The principle underlying x-ray diffraction is Bragg's equation, which relates the wavelength of the incident radiation to the interspacing between atomic planes ("d-spacing") and reciprocal lattice. [38]

$$2d \sin \theta = n\lambda \quad (1.18)$$

Where n (an integer) – 'order' of reflection,

λ – wavelength of the incident X-rays,
 d – interplanar spacing of the crystal,
 θ – angle of incidence

X-ray diffraction (XRD) has been extensively used for solving the problem of material identification, crystal structure elucidation and mineral characterization. By measuring the angular 2θ position (angle between the incident and scattered beam) of the various diffraction peaks observed from the graph, it is possible to obtain the interatomic spacing in the material. Since the specific set of values of d 's serve as unique fingerprints, XRD is able to identify not only the presence of specific constituent atoms in a material (in this case the chemistry) but the stoichiometric ratio as well. The advantage of this is that we can distinguish between different phases of a material (for example, the rutile, anatase or brookite forms of TiO_2).

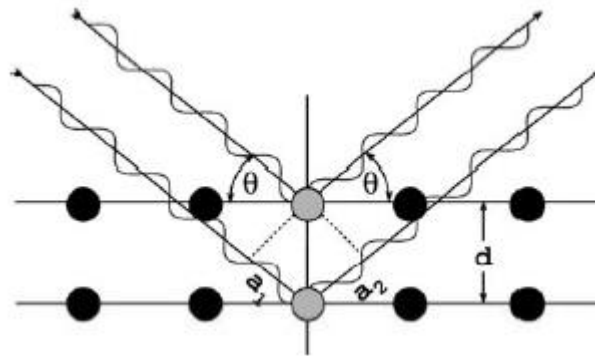


Figure 1.7 Geometric derivation of Bragg's law: Constructive interference occurs when the delay between waves scattered from adjacent lattice planes given by $a_1 + a_2$ is an integer multiple of the wavelength λ . (that is, when the waves are in alignment) [39]

1.4.2 Scanning electron microscopy (SEM)

Scanning electron microscopy (SEM) belongs to a class of surface analytical techniques whose underlying principle is based on the detection of particles emitted from a sample that has been irradiated with a finely focused beam of electrons. The incident beam of electrons hits and interacts with the material, thus producing a huge number of signals, i.e. electrons and X-rays are emitted from the specimen. A detector converts the signal to images which are dependent upon the chosen magnification. A typical SEM instrument consists of an electron gun (usually made of a tungsten filament or lanthanum hexaborate, LaB_6), a vacuum and a column. The latter holds the condenser lens, scanning column, stigmator, detector, and the sample holder [40].

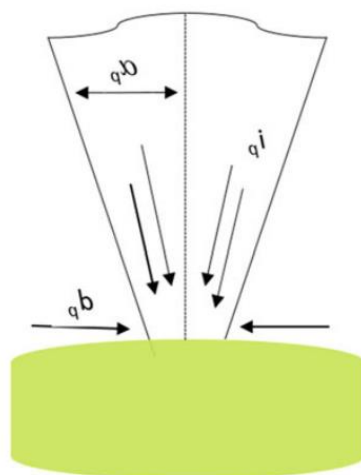


Figure 1.8 The parameters of the electron beam with the greatest impact on the sharpness, resolution and visibility of SEM images are the electron probe size (d_p), electron probe current (i_p) and electron probe convergence angle (α_p). [41]

With a useful magnification of about 200,000X, the scanning electron microscope can provide rapid imaging of the external morphology of materials. The advantages of this method include large depth of field and variety in the type of specimen that can be examined. One major drawback, however, is that samples have to be conducting to avoid artefacts resulting from a build-up of charge [41]. The choice of accelerating voltage is paramount here as increasing the voltage might induce charging in non-conductive samples. This presents some difficulty when examining biological samples and other non-conducting materials. To get around this, we have to coat, via sputtering, the surface of the sample with a layer of metallic film.

The scanning electron microscopy offers various tools that can lead to a better understanding of the material being examined. Such tools include

- i. Back scattered electrons (BSE) which are used to identify the crystallographic phases in the material.
- ii. Secondary electrons (SE) used in the elucidation of the material topography.
- iii. Energy dispersive X-ray (EDX) used for elemental composition analysis.
- iv. Electron beam induced current (EBIC) for monitoring the current path in optoelectronic materials and to estimate the homogeneity of the sample.

1.4.3 Photoluminescence (PL)

Photoluminescence spectroscopy is used to study electronic defects. It is a useful criterion for assessing the recombination efficiency of photogenerated electrons and holes in photocatalytic reaction. The phenomenon of photoluminescence is associated with materials that are capable of absorbing energy and then re-emitting visible light as

they undergo electronic relaxation. Luminescence is one of the optical processes associated with the emission of radiation from semiconductors, the other one is the inelastic scattering of light. Because imperfections and defects within the sample interfere with the recombination processes, photoluminescence is able to provide information about the optical characteristics of a semiconductor[42].

The main components of a PL spectrometer are:

- i. Light source which serves as an excitation source
- ii. Excitation monochromator which selects specific monochromatic light from the incident light
- iii. Sample chamber for optical components and sample holder
- iv. Emission monochromator
- v. Detector
- vi. Screen/monitor

Photoluminescence is usually used in combination with other techniques like the scanning electron microscopy to characterize nanomaterials and nanocomposites. Other applications include the determination of the distribution of phases in binary, ternary and quaternary compounds. In this study, photoluminescence was used to study the defect nature of the ZnO_R layers.

1.4.4 X-ray photoelectron spectroscopy (XPS)

X-ray photoelectron spectroscopy is a common method used to probe the surface properties of samples. It belongs to a class of emission spectroscopy technique, together with atomic emission spectroscopy (AES) and inductively coupled plasma-atomic emission spectroscopy (ICP-AES)[40]. XPS can probe the top 30 to 100 atomic layers of a surface and identify the chemical state of those layers, whether they be elemental or part of a molecule. XPS's applications are in the study of materials whose surface and interfaces play a great role in reactivity, for example, in the study of photocatalysts, semiconductor materials, and coatings [43][44][45][46].

As the name suggests, XPS is based on the photoelectric effect (Figure 1.9). During the photoelectron emission process, an incident photon of energy $h\nu$ is absorbed by an atom. With that energy, a photoelectron is emitted with kinetic energy according to equation 1.19.

$$KE = h\nu_{known} - BE - \Phi_{spectrometer} \quad (1.19)$$

Where BE - binding energy of the electron,

$\Phi_{spectrometer}$ - work function of the spectrometer

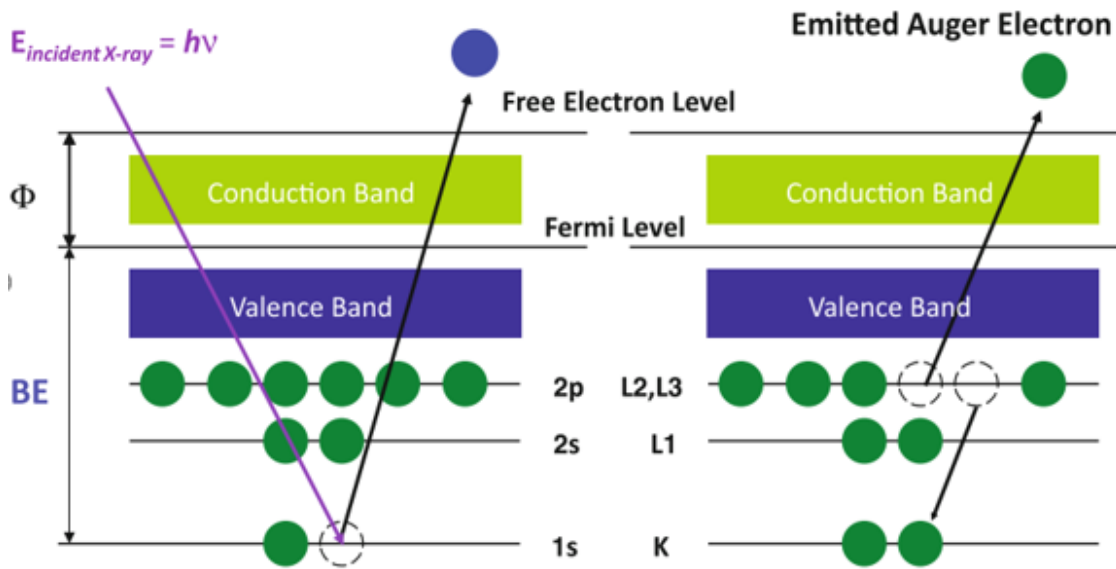


Figure 1.9 Photoelectron and Auger electron emission process [55]

When a second electron is emitted upon relaxation instead of an X-ray photon or an X-ray fluorescence, the process is known as Auger emission spectroscopy. The output of an X-ray photoelectron spectroscopy is a chart of signal(cps) on the y-axis and binding energy (eV) on the x-axis. The binding energy depends on the atomic number, Z , which is a characteristic of every element. XPS was used in this study to examine the chemical composition of the surface of the ZnO nanorod layers. From this, we are able to estimate the relative amount of hydroxyl groups on the surface.

1.4.5 UV – Vis spectroscopy

Ultraviolet (UV) and visible light (Vis) spectroscopy is the most common method employed in photodegradation studies.[47][43][24] This works by measuring the concentration of the residual organic components in the dye solution via absorption using a UV-Vis spectrophotometer[48].

When a monochromatic light source is used, Beer's law gives the relationship between absorbance and the concentration of the absorbing species.

$$A = \epsilon bc \tag{1.20}$$

Where b - path length in centimetres,

ϵ is the molar absorptivity in $\text{L mol}^{-1} \text{cm}^{-1}$,

c is the concentration in moles per litre[41].

As the concentration of the chromophore in the sample decreases, the absorbance decreases as shown in Figure 1.10.

Organic compounds contain unsaturated functional groups (chromophores) which absorb radiation with wavelengths in the range of (200 to 700 nm). This absorption leads to transitions of the n electrons to the n^* excited state[41]. The efficiency of photodegradation (also known as the decolorizing ratio) is determined using the following equation:

$$\text{Degradation efficiency(\%)} = \frac{C_0 - C}{C_0} \times 100 \quad (1.21)$$

Where C_0 - solution concentration at $t = 0$,

C - solution after some irradiation time.[49][50]

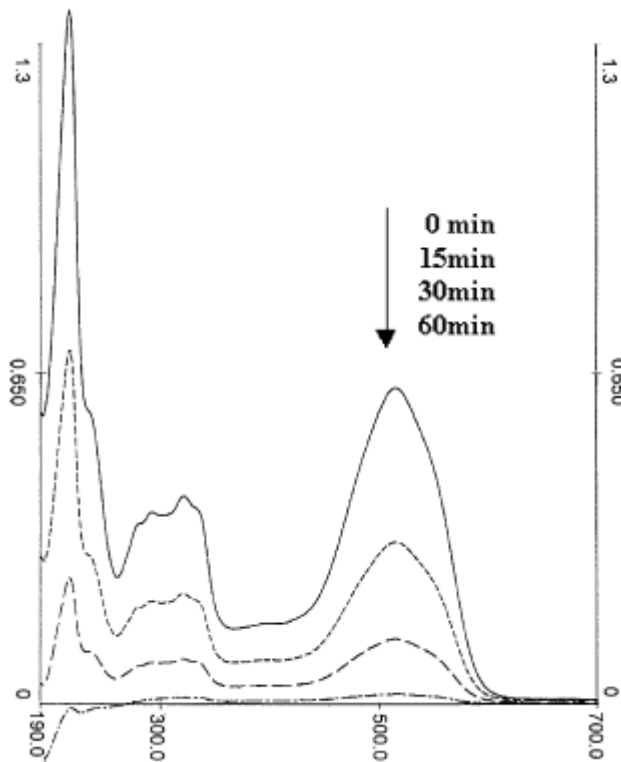


Figure 1.10 UV-Vis spectra changes of AR14 (20 ppm) in aqueous ZnO dispersion (ZnO 160 ppm) irradiated with a mercury lamp light at pH neutral, at times: (1) zero, (2) 15 min, (3) 30 min, and (4) 60 min where ppm = mg/kg \approx mg/L = g/m³. [51]

Uv - Vis Spectrometers are also used in the optical characterization (determination of the bandgap) of semiconductors. By obtaining the values the transmittance and absorbance of the material, we can determine the bandgap of the sample with the aid of a Tauc's plot.

1.5 ZnO properties

Zinc oxide is a II^b-IV compound semiconductor material. ZnO has a wide direct bandgap and large exciton binding energy of 60 meV [52]. Its direct bandgap energy of 3.37-3.4 eV [53] is in the UV spectral range and thus makes it transparent to visible light. Its large exciton binding energy provides ultraviolet (390 nm) excitonic laser action upon pumping at room temperature providing ZnO with excellent luminescent properties and making it a promising material for the development of optoelectronic, spintronics and photovoltaic devices.



Figure 1.11 Crystal structure of $2 \times 2 \times 2$ supercell wurtzite ZnO [54]

Table 1.4 Properties of wurtzite ZnO [55]

Properties	Value
Lattice constants (T = 300K)	
a_0	0.32469 nm
c_0	0.52036 nm
Density	g/cm^3
Melting point	2242 - 2248K
Relative dielectric constant	8.66
Gap Energy	3.4 eV
Intrinsic carrier concentration	$< 10^6 \text{ cm}^{-3}$
Exciton binding Energy	60 meV
Electron effective mass	0.24
Electron mobility (T = 300 K)	$200 \text{ cm}^2/\text{V s}$
Hole effective mass	0.59
Hole mobility (T = 300 K)	$5\text{-}50 \text{ cm}^2/\text{V s}$
Cohesive energy per bond	7.52 eV
Molar mass	81.37 g/mol

ZnO is similar to TiO₂ in terms of eco-friendliness, photocatalytic activity, and the ease of synthesis. In addition, ZnO is an earth abundant material [34]. The main properties of ZnO are summarized in Table 1.4.

1.6 ZnO structure

The crystal lattice binding of ZnO gives rise to sp³ hybridization with the electron states occupying four orbitals directed in the corners of a tetrahedron. This tetrahedral coordination gives ZnO its characteristic geometry where each anion is surrounded by four neighbouring cations. This tetrahedral geometry is stabilized by the angular rigidity of the binding sp³ orbitals. This tetrahedral arrangement of tetrahedrons usually gives rise to either a cubic zinc-blende-type structure, a rocksalt (NaCl) structure or in a hexagonal wurtzite-type structure depending on how the bilayers of zinc and oxygen are stacked in the sequence (Figure 1.12). Under ambient conditions, the wurtzite remains the most stable phase. The higher bond polarity is responsible for this favoured stability. However, the zinc blende ZnO structure can be stabilized through epitaxial growth on zinc-blende-type substrates, while the rocksalt structure may be obtained under relatively high pressures [53].

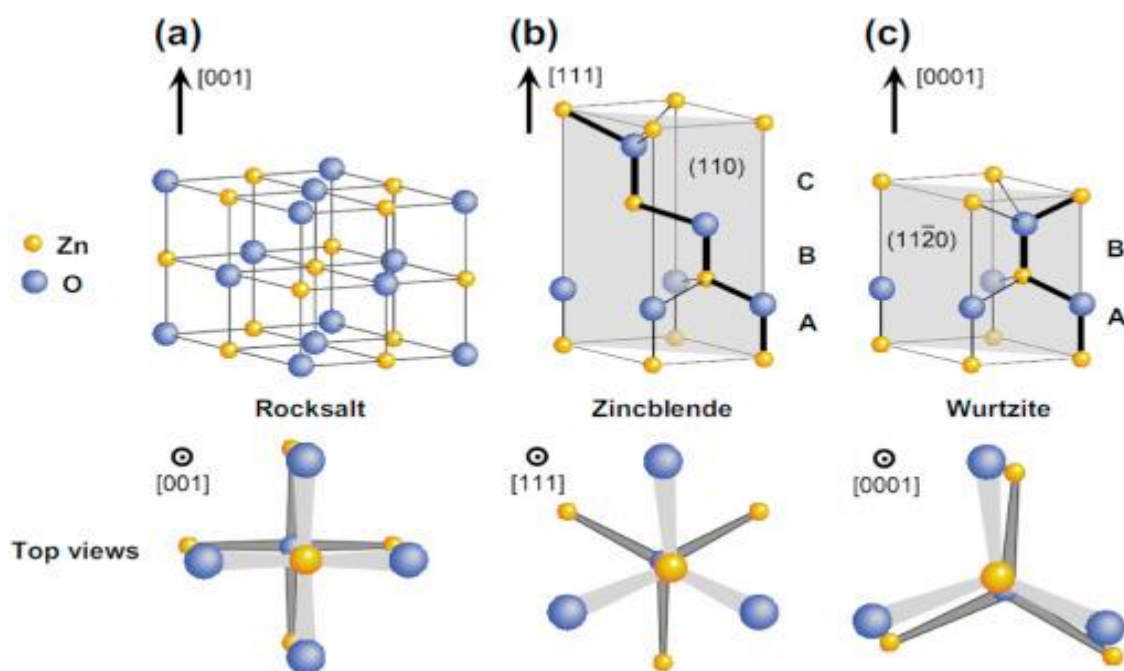


Figure 1.12 Ball and stick representation of ZnO crystal structures: (a) cubic rocksalt (B1), (b) cubic zincblende (B3) and (c) hexagonal wurtzite (B4) [56]

Wurtzite ZnO is a classic polar crystal. Two types of wurtzite Zn (0001) surface structures exist, namely, Zn-polar surfaces with O-atom terminations and O-polar

surfaces with Zn-atom terminations. In this study the ZnO nanorods grown via hydrothermal synthesis are of the wurtzite type crystals.

1.7 Nanostructured ZnO

A significant amount of research is concerned with nanostructured ZnO materials because of their distinguished performance in electronics, optics, and photonics [52]. ZnO can be synthesized into nanostructures with different morphologies. They could be in the form of microballs [57], nanorods [58], nanowires [59], nanoflowers [60], and nanodisks [61]. The ease of synthesis of ZnO into different morphologies allow for the tuning of its properties. Among these various structures, there is especially a high level of activity in the study of one-dimensional (1D) materials due to their high and active surface area. These class of materials have been widely studied for their potential applications in energy conversion and the degradation of environmental pollutants. Zinc oxide nanorods usually grow vertically in a direction perpendicular to the (0001) plane. This is because, while ZnO nanostructures display anisotropy. The growth rate of individual crystallographic planes is determined by the energy minimization principle and follows the order: $v(0001) > v(10\bar{1}0) > v(10\bar{1}\bar{1}) > v(10\bar{1}1) > v(000\bar{1})$. Since the most energetically favourable orientation is the (0001) plane, a rodlike shape becomes the most probable [62].

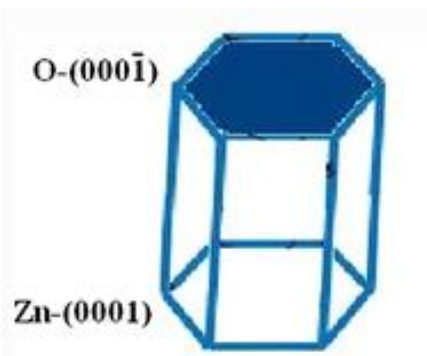


Figure 1.13 ZnO_R morphological model showing the top surface of O-(0001⁻) terminations and the bottom surface of Zn-(0001) terminations.

1.8 Applications of ZnO

ZnO is a material widely used in various fields. Currently, up to 100,000 tons of ZnO are produced per year [56]. A large proportion of this production is used in the cement industry where ZnO is added as an additive to concrete to prolong the latter's setting

time. ZnO is also used as a white pigment in paints and is preferred over Pb containing paints since it is not toxic and does not react with hydrogen sulphide [53].

Because of its photostability and high UV absorption, ZnO is employed as an absorber in sun blockers. In medicine, ZnO is widely used for its anti-microbial and anti-inflammatory properties. The unique properties of ZnO has enabled its use in various materials both past and present. The intrinsic sensitivity spectrum for photoconductivity of pure ZnO begins in the near UV region because of its wide bandgap. Thus, ZnO has been employed as a photoconducting material within this spectral range. This unique effect was widely applied in the electro fax photocopy process.

Over the past few years, there has been a sustained ZnO research activity with the hope of obtaining a ZnO-type alternative to the group III-Nitrides for a blue optoelectronics. One advantage over GaN in this regard is the ability to grow single crystal substrates. In addition, ZnO has the advantage of being insensitive against high energy radiation (MeV range) making it suitable for all applications in electronics. Its surface conductivity can be strongly modified, enabling it to act as a gas sensor. Furthermore, ZnO can be easily doped with n-type elements to concentrations beyond 10^{20} cm^{-3} to form transparent conducting oxides (TCO). A common example is ZnO/Al also called AZO, which has been used as TCO contacts to drive an organic O-LED.

It is worth remarking here that the catalytic properties of ZnO have been known since decades. Nanostructured ZnO is a prominent photocatalyst used in the degradation of pollutants and other organic pollutants. It is sometimes preferred over TiO_2 due to its low-cost, non-toxicity and more efficient absorption across the solar spectrum.

1.9 ZnO by hydrothermal growth

The growth of ZnO nanostructures can be achieved via various synthesis routes. ZnO nanorods have been synthesized via evaporation, chemical vapour deposition, thermal decomposition, wet chemical methods (electrodeposition, spray pyrolysis), solvothermal methods, hydrothermal and microwave-assisted methods.

Hydrothermal growth is a technique for the deposition of semiconductor material using liquid under pressure. The advantages of the hydrothermal method are a low growth temperature, a DT close to zero at the liquid/solid interface, and an easily scalable technique [63]. Hydrothermal synthesis is regarded as a green chemistry technique because hydrothermal reactions occur at low temperatures, water can be used as a solvent and wastage is minimized as the reaction occurs in a sealed environment. As well as being simple, the method is practical and thus suitable for one-step synthesis of ZnO nanostructures [64]. Besides its use in the synthesis of nanoparticles, hydrothermal bulk growth serves as the most promising technique for fabricating ZnO wafers [53].

Figure 1.14 outline the steps involved in the synthesis of nanomaterials via hydrothermal synthesis.

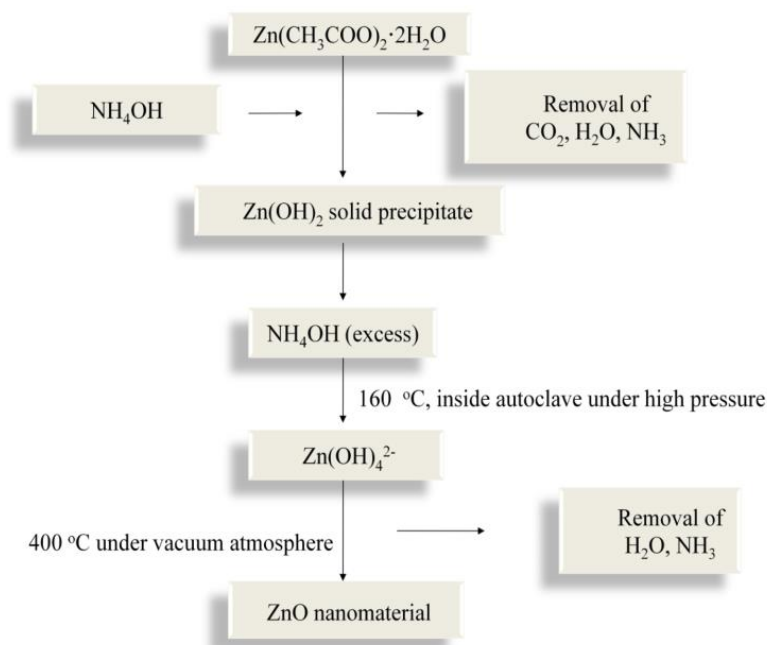


Figure 1.14 Schematic diagram of the preparation of ZnO nanomaterials by hydrothermal synthesis route [65]

Hydrothermal methods are suitable for the synthesis of metallic nanoparticles and have been shown suitable for the growth of large ZnO crystals from aqueous basic (OH^-) solutions at temperatures less than 500°C . Typical growth conditions as described by literature are dissolution zone temperature of $270 - 350^\circ\text{C}$, temperature difference between the growth and the dissolution zone, $\text{DT} \sim 20\text{-}80^\circ\text{C}$ and pressures between $15 - 140 \text{ MPa}$ [63]. An increase in both residence time [66] and precursor concentration has been found to increase the average particle size as well as the particle size distribution of the nanoparticles formed.

1.10 Literature overview on ZnO rodlike crystals grown by hydrothermal method

In the synthesis of ZnO_R via hydrothermal methods, it is customary to vary the synthesis protocols in terms of the starting materials, pH, temperature and the methodology of precursor preparation. These factors control the supersaturation which is responsible for an increase in nucleation and growth rate such that when growth rate dominates over the nucleation rate, the crystallite size increases. However, crystallite size decreases as the nucleation rate dominates. Precursor concentration also affects the density of the

nanorods distribution while deposition time, pH, and temperature have much greater influence on the aspect ratio of the nanorods [66].

1.10.1 Influence of precursor type, concentration, and pH on ZnO crystal morphology

Suchanek [67] succeeded in demonstrating that within the temperature range of 160-280°C, the optimum combination of pH and concentration, which was required to obtain pure-phase ZnO crystals appeared to be 9-14 and 1-4 mol/L respectively. They found that zinc concentrations in excess of 1 m result in a high production yield while significantly lower concentrations do not. Lu and Yeh [68] studied the effect of the pH of the precursor solutions on the growth of ZnO crystals. The pH of the starting solutions was adjusted from 9 to 12 before the commencement of the hydrothermal procedure. The authors found that a higher pH favoured dissolution as all precursors completely dissolved at $\text{pH} \geq 11$. XRD patterns further revealed that the ratio of the intensity of (100) peak to that of (002) peak increases with increasing pH. This was attributed to an increase in the crystallinity of the ZnO crystals since the zinc ion concentration in the bulk solution increases. Thus, a higher pH range favours the growth of a rodlike morphology. From $\text{pH} = 9$ to $\text{pH} > 11$, the shape of the particle changes from ellipsoidal to rodlike as revealed in Figure 1.15.

Another effect of increasing pH is a high aspect ratio since a higher pH favours growth along the a-axis. The authors also observed an inverse relationship between pH and the production yield of the ZnO crystals. At a $\text{pH} \geq 12.5$, the nucleation of ZnO particles becomes difficult since all zinc hydroxide precursors are dissolved, leaving a clear homogeneous solution. ZnO is an amphoteric compound and will dissolve in strongly alkaline solution. This makes it hard to obtain a supersaturated concentration and consequently, nucleation. One important constraint noted by Suchanek is the difficulty in elucidating the effects of pH and concentration since hydrothermal supersaturation reaches a maximum at different combinations of pH and concentration for different zinc salt precursors. In other words, it would require a comprehensive study of varying concentration and pH while keeping all other parameters constant to fully understand the effect of pH and concentration during the hydrothermal synthesis of ZnO crystals. This work by Lu is in agreement with that carried out by Polsongkram et al. [69] In the latter's hydrothermal synthesis of ZnO nanorods they varied the concentration of the precursor $\text{ZnNO}_3\text{-HMTA}$ from 0.005 mol/L:0.005 mol/L to 0.05 mol/L:0.05 mol/L at 75°C. It was observed that increasing the concentration of the aqueous precursor solution resulted in nanorods with a higher surface to volume ratio. On the contrary, wider nanostructures were obtained for lower concentration ratios of ZnNO_3 to HMTA.

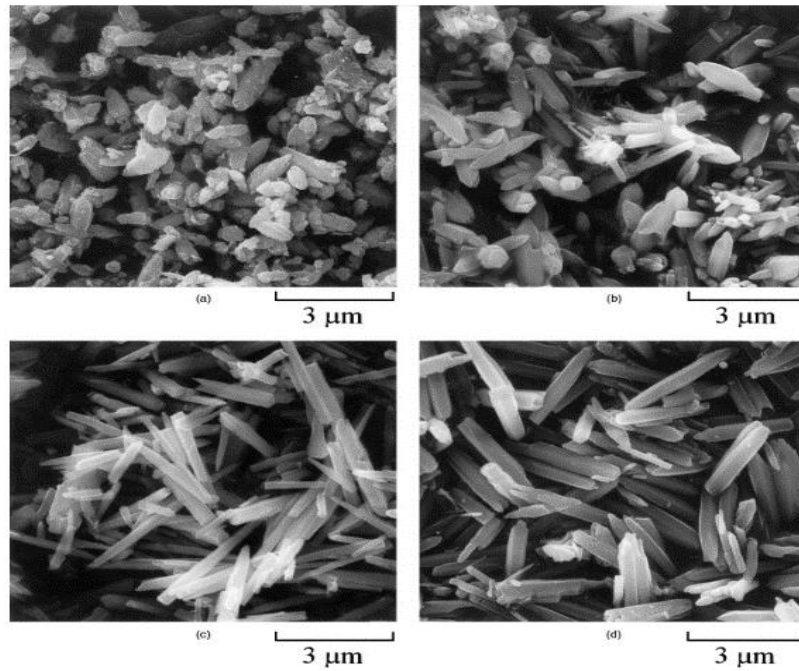


Figure 1.15 SEM images showing morphology of ZnO crystals prepared at varying pH = (a) 9, (b) 10, (c) 11, and (d) 12 [68]

1.10.2 Influence of synthesis time on the hydrothermal growth of ZnO crystals

Lu and Yeh [68] also studied the effect of time on the hydrothermal growth of ZnO crystals. For this, they fixed the reaction temperature at 100°C and varied the reaction time from 0 – 2 h. They observed very little variation of particle shape with reaction time. However, a different scenario was seen for the yield. The authors noted a slight increase in the yield with reaction time from 76% at 0 h to 83% at 2 h. Work done by Polsongkram et al. [69], confirms the invariant nature of hexagonal nanorod shape with the deposition time. However, they observed an increase in the size and density of the nanorods with increasing reaction time – a phenomenon known as “Ostwald ripening” [70][71]. Figure 1.16 illustrates the phenomenon of Ostwald ripening. Figure 1.16 (a) shows flake-like particles formed after 15 mins. After 60 minutes Figure 1.16 (c), the nanoparticles have been transformed into rods.

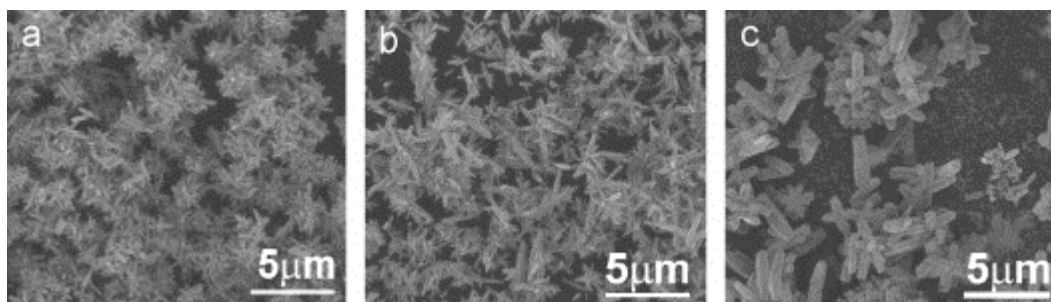


Figure 1.16 SEM images showing the influence of time on the hydrothermal growth of ZnO crystals. Using ZnNO_3 -0.04 mol/L: HMTA-0.025 M at 75°C: a) 15 min, (b) 30 min and (c) 60 min [69]

1.10.3 Influence of hydrothermal temperature on the morphology of ZnO crystals

Temperature is a crystal growth rate-controlling factor. Thus, an increase in temperature leads to a faster decomposition and dissolution of precursors. When the hydrothermal temperature is increased, hexamethylenetetramine (HMTA) rapidly decomposes and produces OH^- ions. This causes the ZnO to grow into nanorods having a larger diameter than nanorods synthesized at lower temperatures [62]. Under low-temperature conditions, the decomposition of HMTA proceeds at a uniform mild rate hindering the adsorption and consequent preferential attachment of ZnO at the top and sides which usually favours uniform growth and thickness [72].

According to Suchanek [67], increasing the synthesis temperature (160 -280°C) within a pH range of 9.6 and 12, caused the formation of larger ZnO crystallites irrespective of the concentration of the precursor used. It should be noted that temperatures greater than 150°C can result in rapid growth of the nanostructures and subsequent depletion of Zn ion reserves. This factor hampers the formation of full-shaped nanorods and leads to crystals that are more needle-like. The study undertaken by Lu and Yeh [68] in which the hydrothermal synthesis of ZnO crystals was carried out at 100, 150, and 200°C for 2h confirms the preceding observation. The particle size was found to decrease with increasing temperature – 1.25mm at 100 and 150°C to 0.85mm at 200°C.

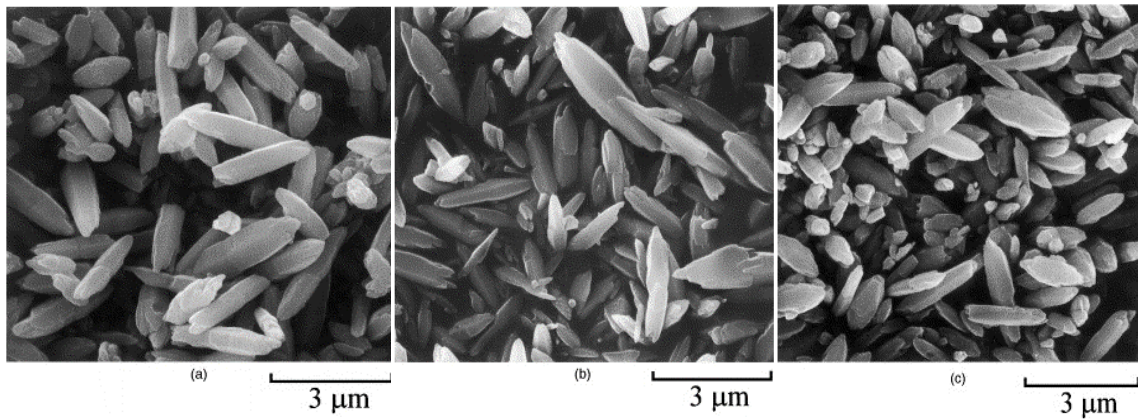


Figure 1.17 SEM images of ZnO powder hydrothermally prepared at (a) 100°C, (b) 150°C, and (c) 200°C for 2 h. [68]

1.10.4 Influence of a seed layer

The deposition of a seed layer of ZnO has been demonstrated to encourage the growth of highly structural and oriented ZnO nanostructures. The importance of seed layer deposition on the growth orientation of ZnO crystals has been widely emphasized in the literature [73]. Several methods are usually employed in the deposition of the ZnO thin films on the glass substrate. They include magnetron sputtering, dip-coating, spin-coating, spray pyrolysis, sol-gel and atomic layer deposition. The liquid-phase methods have the advantages of simplicity and low-cost; hence they are widely employed. The consensus is that the seed layer provides heterogeneous nucleation sites for the growth of the ZnO crystals. The higher the number of seed layer crystallites having their (0001) plane exposed to the precursor solution, the more favorable will be the columnar growth of the nanorods [74]. S Kardeş and Öztürk [75] reported the ZnO seed layer effect on the growth of ZnO nanorod arrays. By using seeded glass substrates made from zinc acetate precursor solution with and without polyvinyl alcohol (PVA), the authors were able to determine the role of precursor chemistry in nanorod alignment. It was observed that using an adequate amount of PVA made it possible to grow vertically aligned nanorods.

Although no significant improvement was noted in photocatalytic activity compared to randomly oriented nanorods. It was also pointed out by Karaköse and Çolak [76] that the seed layer morphology impacts on the structural and electrical properties of the ZnO nanorods. By investigating the effect of seed layers coated on glass substrates via ultrasonic spray pyrolysis, the authors showed that a homogeneous seed layer surface motivated the growth of highly uniform and oriented ZnO nanorods. The report by Gerbreder et al., [62] confirms the role of seed layer in morphology control. Gerbreder et al., obtained seed layers via magnetron sputtering (MS), electrolytic deposition (ED)

and by using zinc acetate colloidal ethanol solution (AD). The SEM images from their study as shown in Figure 1.18 reveal that without a seed layer, the ZnO grows into thick and disordered crystals. However, the ZnO crystals grown on seed layers form a homogeneous and dense array, emphasizing the crucial effect of seed layers in governing morphology and structure. In this study ZnO seed layers were coated on glass substrate using ultrasonic spray pyrolysis method (USP) and allowed to grow vertically, oriented towards the c-axis.

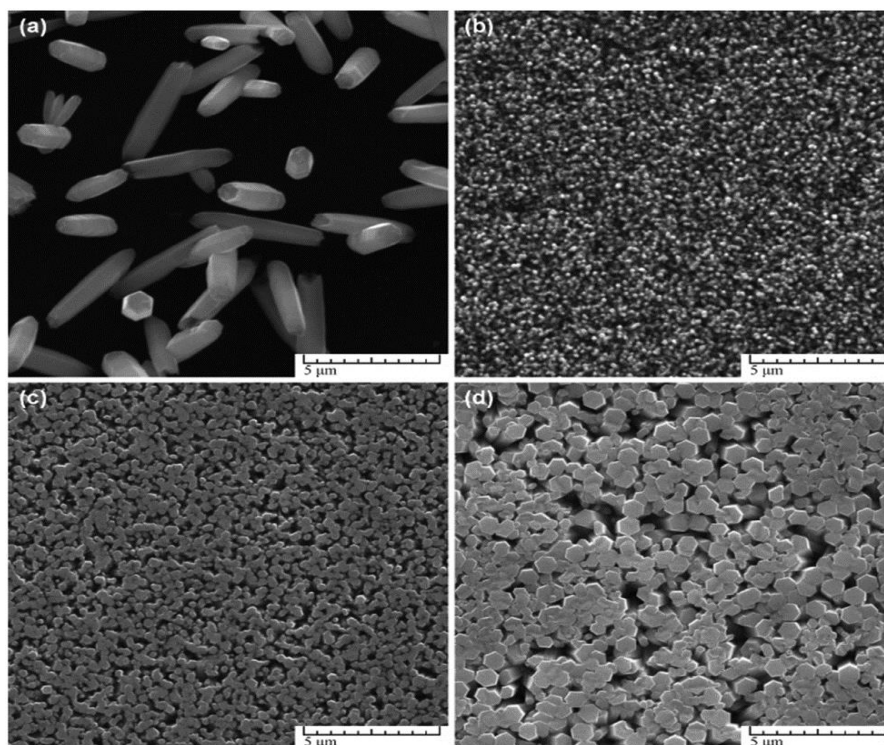


Figure 1.18 SEM images showing ZnO nanostructures synthesized at different origin of seed layer: (a) on clear glass, (b) on MS seeds, (c) on ED seeds, (d) on AD seeds. Other parameters were: 0.1 M $Zn(NO_3)_2$ + HMTA equimolar solution, $t = 3$ h, $T = 90$ °C [62]

1.11 Summary of literature review

Table 2.1 provides a summary of different ZnO morphologies synthesized via hydrothermal methods. The nanostructures range from nanoflowers to nanorods. A large proportion of the studies reviewed in the table used zinc acetate as the source of zinc ions. Diameters of nanostructures were in the μm to nm range, while the photocatalyst quantity was between 5 mg/L to 0.5 g/L. There was also variation in the amount of dye degraded in the studies. Overall, degradation efficiency spanned 67 % to 100 %. It is thus evident from the table that many parameters were varied which makes a comparison of the activity of different photocatalyst quite unfeasible.

Table 1.5 Photocatalytic activity comparison of various ZnO morphologies fabricated by hydrothermal method

Structure	Precursor	Size	Qty	Dye Conc	Radiation	Degradation	Time	
Nanoflowers	Zinc acetate dihydrate + KOH	diameter = 2-4 μm	1.5g/L	100 ml of 10 mg/L MB	UV	93%	60mins	[77]
Mesoporous crystals	Zinc nitrate hexahydrate + PrN3O9.H2O	crystallite size of 23.35 nm	5 mg/L	10 ml of RhB	UV/Visible	93.75% for 6.0mol% Pr-doped	45mins	[78]
Microcrystals	Zinc acetate dihydrate + Methanol	diameter = ~60-90 nm, length = 1.5-3 μm	40 mg/L	40 ml of (200, 100,50, 25, 12.5 and 6.5 ppm)	UV	0.026, 0.042, 0.043 min ⁻¹ for 200, 100,	60mins	[79]
Nanorods	Zinc nitrate hexahydrate + HMTA	diameter of ~200nm 1.5-3 μm	1cm ²	1.0 \times 10 ⁻⁵ M MB Solution	Visible	73% 93%	240mins	[80]
Nanoflowers	Zinc nitrate hexahydrate + NaOH + n-butanol + CTAB,	diameters around ~15 μm	20 mg/L	20 mL of 10 mg/L RhB	Visible	67% 94%	180mins	[81]
Nanorods	Zinc nitrate hexahydrate + KOH +HCl + NaOH	length = 100 nm, diameter = 10-15 nm	100 mg/L	20-120 mg/L MB	UV	98%	60 mins	[34]
Mesoporous crystals	Zinc nitrate hexahydrate + indium sulphate +	crystallite size of 19.08-28.91 nm	0.5 g/L	100 ml of 10 ⁻³ mol/L MB	Visible	80%	120mins	[82]
Nanospheres	Zinc nitrate hexahydrate + KOH + ethylene glycol	diameter 200-250 nm	10 mg/L	100 ml of 10 mg/L MO	UV	100%	90mins	[83]
Nanostructures	Zinc nitrate hexahydrate + Hexalene glycol +	length = 150nm	0.03g/L	40ml of 5mg/L RhB	Visible	100%	80mins	[84]

1.11.1 Aims of the study

Work in the area of photocatalytic degradation is extensive but is primarily concerned with the variation of different intrinsic and extrinsic parameters and conditions. There is no direct study investigating the effect of a photocatalyst on the degradation of different pollutants under similar conditions. Therefore, this study is concerned with the

1. Synthesis of ZnO_R layers via hydrothermal growth
2. Study of the morphological, structural, optical characteristic as well as surface composition of the as synthesized ZnO_R layers.
3. Study of the photocatalytic properties of the as synthesized ZnO_R layers using three different organic dye pollutants while keeping the dye concentration, and other parameters constant.

2. EXPERIMENTAL PART

2.1 Materials and methods for samples preparation

Zinc oxide nanorods (ZnO_R) samples were synthesized in two stages namely,

1. Preparation of homogeneous and uniform ZnO seed layers
2. Hydrothermal growth of ZnO nanostructures.

The hydrothermal chemical reactions showing the proposed growth mechanism of ZnO nanorods using HTMA and Zn(NO₃)₂·6H₂O as precursors is as follows [69]:



Soda-lime glass substrates were cut into pieces of size of 38x9x1.1 mm. This was followed by a thorough cleaning procedure. First, the glass substrates were pre-cleaned with detergent solution, and then cleaned with deionized water (DI), isopropanol in an ultrasound bath. The substrates were subsequently dried and washed repeatedly with DI water. Properly cleaned glass substrates were placed onto heated tin molten bath for deposition of the ZnO seed layer. ZnO seed layers have been previously deposited by ultrasound spray pyrolysis method [76][85][86][87]. The apparatus set-up is shown in Figure 2.1.

Precursor solution was nebulized with the help of a pneumatic spray head, operating in pulsating feeding mode (5 seconds feeding, 20 seconds pause). Spraying solution composed of 0.05 mol/L Zn(ac)₂ solution in 2/3 vol% of isopropanol/water mixture. 20 ml of precursors solution was sprayed over the 5 samples simultaneously. Bath temperature (T_s) was fixed to 500 °C. Air-flow rate was adjusted to 8 L/min. According to SEM, seed layer morphology represented flat and compact structure composed of roundly shaped 30 nm thick crystals. The thickness of the whole seed layer was ca. 80 nm.

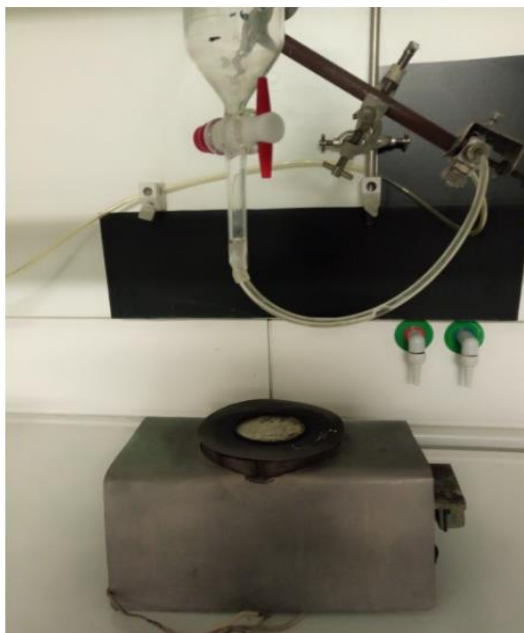


Figure 2.1 Image of a spray pyrolysis equipment – courtesy of thin film laboratory technology - Taltech

However, it is well-known that ZnO nanorods formation is highly sensitive for specific substrate; therefore, before the study, we had tested various concentrations of main precursors, temperatures and deposition times. For our specific seed layer, the optimal concentration to produce elongated high open surface area nanorods was found to be 0.1 mol/L. For the hydrothermal synthesis, 5 seeded glass substrates were simultaneously mounted in 40 ml reactor beaker with a precursor solution containing equimolar concentrations of zinc nitrate hexahydrate ($\text{Zn}(\text{NO}_3)_2 \cdot 6\text{H}_2\text{O}$; Sigma-Aldrich, 99.9 %) and hexamethylenetetramine ($(\text{CH}_2)_6\text{N}_4$; HMTA; Sigma-Aldrich) 0.1 mol/L. The ZnNO_3 provides the Zn^{2+} ions while HMTA, a weak base slowly decomposes in the solution, providing an alkaline environment and the desired amount of hydroxide OH^- ions. Then reactor beaker was then mounted into steel autoclave and the reaction was allowed to proceed for 2 h at 120 °C. The autoclave reactor used was a Berghof BR-100 with a Berghof BTC-300 temperature controller (Figure 2.2).

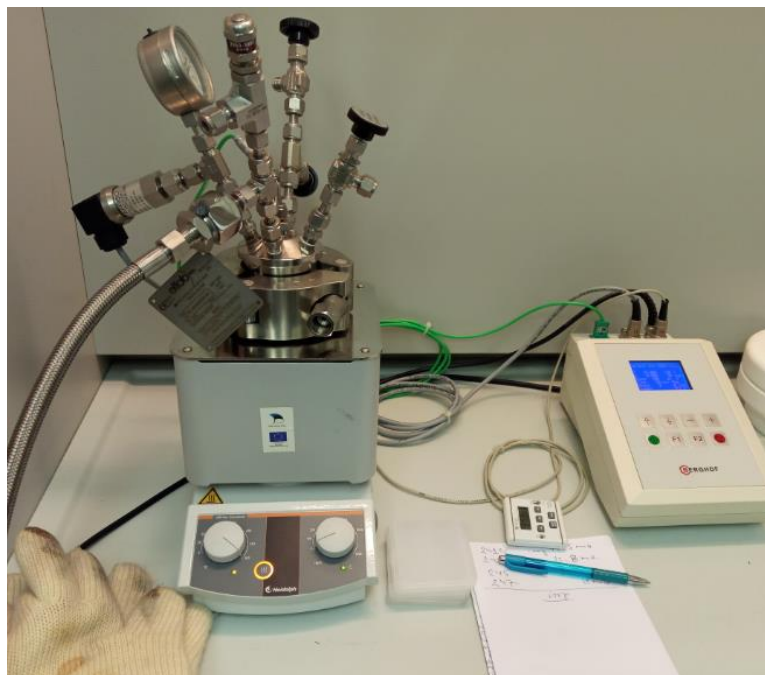


Figure 2.2 Steel autoclave reactor Berghof BR-100 from the Thin film technology laboratory – Taltech

2.2 Characterization

The structure and dimensions of the ZnO_R layers were characterized by high-resolution scanning electron microscopy (SEM; Zeiss HR FESEM Ultra 55) with the operating voltage set at 10 kV. Dimensions of the crystals, their average open surface area were calculated from 3 intentionally chosen places from SEM image (plane and cross-sectional views) from area of $2 \times 2 \mu\text{m}^2$. The surface area of one ZnO crystal was calculated according to the cylinder surface area (CSA) formula, excluding one bottom surface, $\text{CSA} = \pi r^2 + 2\pi r h$. The density of the crystals has been counted from $10 \times 10 \mu\text{m}^2$ area. To estimate the mass of ZnO crystals taking part in photocatalytic reaction, we weighed the empty glass substrates and the glass substrate with ZnO_R layer on highly precise balances (sharpness of 0.00001 g). The ZnO film was then cleaned off using an acidic solution. Again, the dried glass substrate was measured. The mass thus obtained had a good correspondence with the initial weight of the freshly-cut glass substrate.

The phase composition and structure were studied on XRD machine. XRD patterns were recorded using a Rigaku Ultima IV diffractometer with CuK α radiation ($\lambda = 1.5406 \text{ \AA}$, 40 kV at 40 mA) and the silicon strip detector D/teX Ultra. The crystalline phases were identified using the XRD reference files (PDF-2 file collection) from the International Centre for Diffraction Data (ICDD, Pennsylvania, US). PDF file numbers for ZnO (zincite) is 00-036-1451.

The optical properties of the photocatalysts were studied on Jasco V-670 UV-VIS-NIR spectrophotometer equipped with an integrating sphere. The spectra were taken in the wavelength range of 300-2000 nm.

In order to study the wettability of the ZnO_R layers water contact angle (CA) measurement was used. Measurements were carried out on a DSA 25 (KRÜSS Instrument) at room temperature, using the sessile drop fitting method. The average of water contact angle from three spots was recorded as the final value.

A KIMMON IK series He-Cd laser with the excitation wavelength of 325 nm (3.8 eV) was used for room-temperature photoluminescence study. The PL spectra were recorded by using a computer-controlled SPM-2 monochromator ($f = 40$ cm) together with a photomultiplier tube and a DSP Lock-In amplifier SR 810.

X-ray photoelectron spectroscopy (XPS) study was performed on the Kratos Analytical AXIS ULTRA DLD spectrometer fitted with the monochromatic Al K α X-rays source and the achromatic Mg K α /Al K α dual anode X-ray source. All the spectra were charge-corrected by taking C1s peak (BE = 285.0 eV) as reference.

Photocatalytic activity of the ZnO_{RS} was studied by the degradation of Methyl orange (MO), Methylene Blue (MB), Rhodamine-B under UV-light irradiation. Dye degradation rate was monitored by changes in its concentration with time. The concentrations of the dye were monitored after each 30 minutes on Jasco V-670 UV-VIS-NIR spectrophotometer. Philips Mercury lamp (15 W, TL-D model, $\lambda_{\max} = 365$ nm) was used as an UV source. ZnO_R photocatalyst samples (substrate surface area of 3,42 cm²) were dipped inside 3.5 ml poly(methyl methacrylate) (PMMA) cuvette containing 3 ml of dye solution. The nanorod surfaces were aligned to face the light source. Initial concentration of MO, MB and RhB solutions was 0.010 mg/L (10 ppm). The standard measurement of concentration of MO took place at wavelength of 464 nm, MB at 668 nm and RhB at 552 [88].

3. RESULTS AND DISCUSSION

3.1 SEM Study - Morphology and dimensions of the ZnO layers

Figure 3.1 shows the surface and cross-sectional SEM images of the photocatalyst, hydrothermally grown ZnO nanorods (ZnO_R) layers immobilized to the glass substrate. High-density hexagonal nanorods were successfully grown on the seeded soda-lime glass substrates. Figure 3.1(a) shows agglomerated clumps of c-axes oriented ZnO nanoparticles on the substrate. There is a dense coverage of elongated ZnO rod crystals with average lengths of the crystals ca. $1\ \mu\text{m}$, and diameters vary from 50 to 150 nm. Vertical orientation of the crystals prevails, indicating nanorods grown on nucleation seeds with the (0001) planes parallel to the substrate. Furthermore, major crystal population have well-defined hexagonal shape and flat (002) top plane termination.

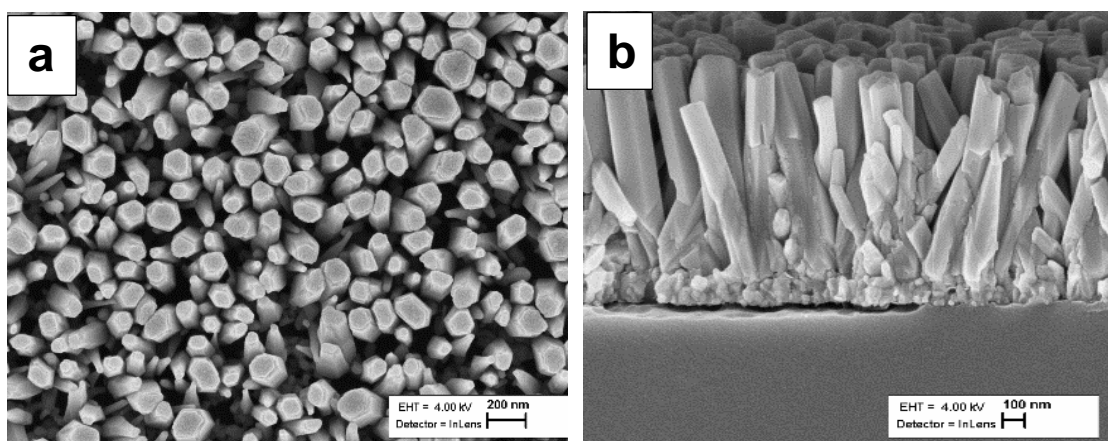


Figure 3.1 SEM images from the surface (a) and cross-section (b) of a ZnO-NR

3.2 XRD study. Structure and phase composition of ZnO layers

According to XRD pattern of the ZnO_R layers shown in Figure 3.2, the main reflections at 2θ of 31.77° , 34.42° , 36.25° , 47.54° , 56.6° correspond to (100), (002), (101), (102) and (110) planes of hexagonal ZnO [PDF file No. 00-036-1451]. Prevailing strong narrow reflection at 34.40° of (002) plane indicates the formation of highly crystalline, c-axis (002)- oriented single-phase hexagonal ZnO crystals are formed. For instance, XRD reflections intensities ratio of (002) and (101) planes of the ZnO_R grown in this

study ca. 58 times higher than that for ZnO powders, being $I(002)/I(101)=58$ for ZnO_R sample compared to ZnO powder $I(002)/I(101)=0.4$ (PDF file No. 00-036-1451). The XRD pattern for ZnO_R layers shows a close resemblance to those reported for strongly c-axis oriented ZnO nanorods produced by hydrothermal and other chemical methods [89][34].

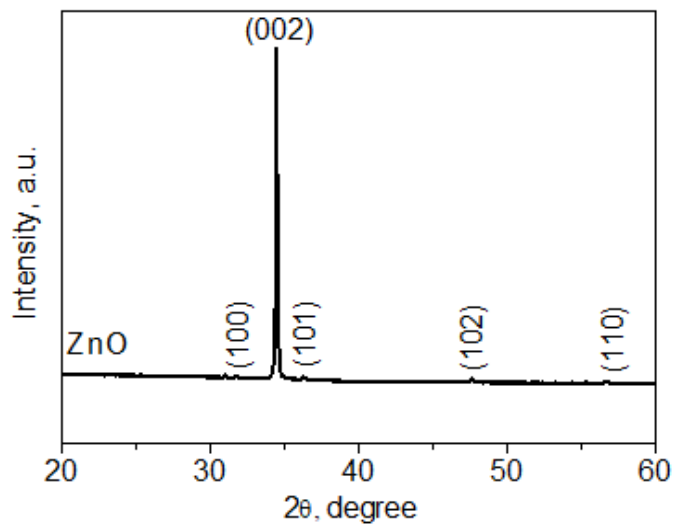


Figure 3.2 XRD pattern of hydrothermally grown ZnOR showing a prominent (002) peak

3.3 UV-VIS Optical Properties

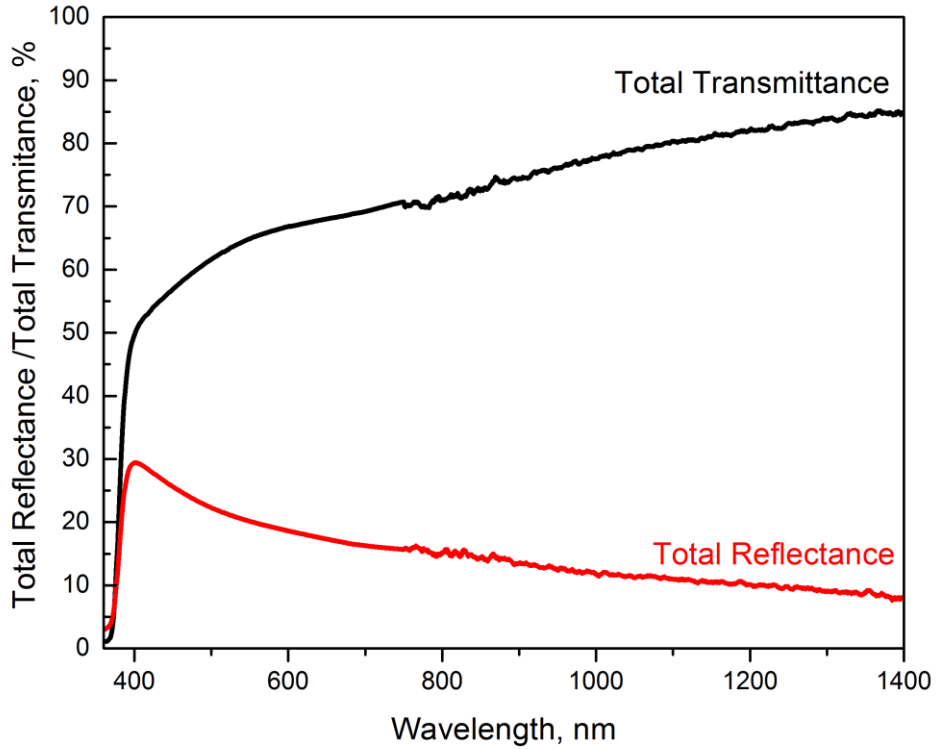


Figure 3.3 Total transmittance (TT) and total reflectance (TR) plots of ZnO_R layers

The total transmittance (TT) plot of ZnO_R reveal a sharp band edge at about 385 nm, which correlates to the bandgap value of ZnO. Total reflectance of ZnO_R, was 35% at 380 nm and gradually decreased to ca. 30% at 550 nm. Such a slump is characteristic of samples containing a fine-grained structure. To obtain the bandgap energy of the layers, it was necessary to determine F(R) using the Kubelka-Munk equation.

$$F(R) = \frac{(1 - R)^2}{2R} \quad (1.1)$$

Where R - the reflectance,

F(R) has a value, which is proportional to the value of the absorption coefficient α in the Tauc equation (1.2).

$$\alpha h\nu = A(\alpha h\nu - E_g)^{n/2} \quad (1.2)$$

Where E_g is the bandgap energy,
 ν is the frequency of light,
 λ is the wavelength of light,

h is Planck's constant,
 α is the absorption coefficient.

Thus, a plot of $\alpha h\nu$ vs $h\nu$, also known as a Tauc plot yields an intercept which represents the bandgap of the material. An estimated value of 3.27 eV was obtained for the ZnO_R using this method. Tauc's plot along with the intercept is presented in Figure 3.4.

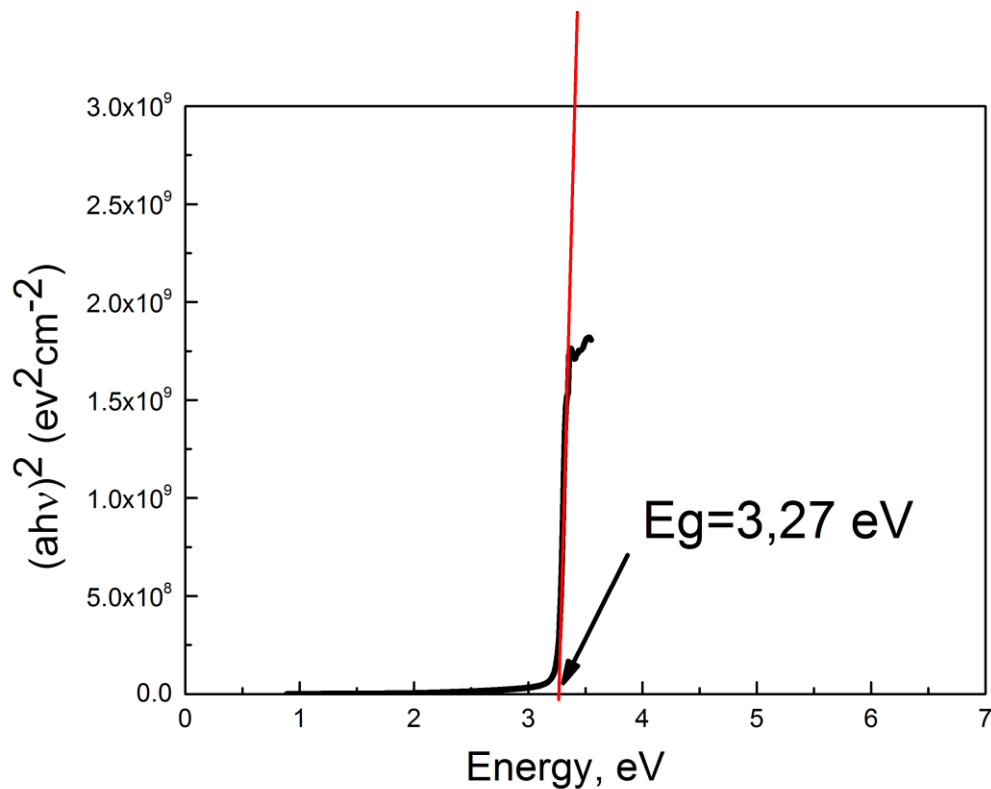


Figure 3.4 $(\alpha h\nu)^2$ vs. energy plot - Band gap (E_g) determination for ZnO layers from Tauc's plot.

3.4 Surface properties of ZnO layers

The surface composition of the ZnO_R layers was investigated by XPS analysis. As the oxygen and carbon species represent the greatest interest for evaluation of presence of the defects, the degree of surface contamination and wetting properties, herein O1S and C1S spectra are included in this study.

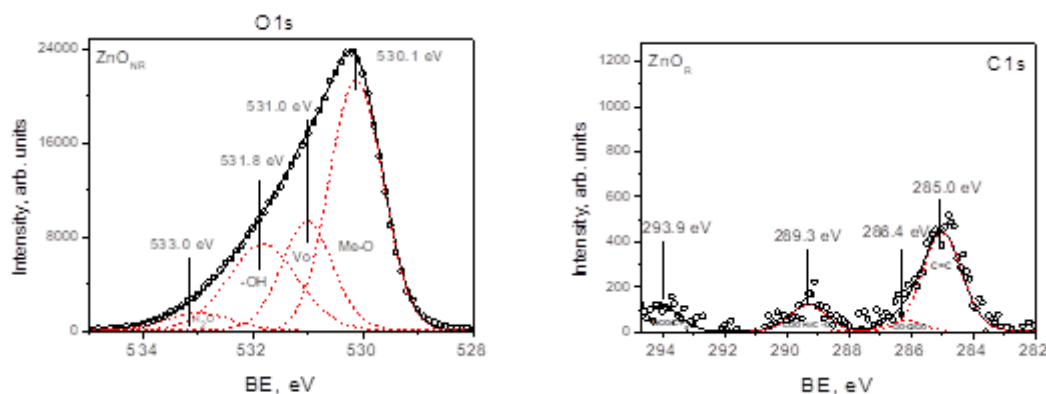


Figure 3.5 ZnOR XPS spectra in the binding energy region of (a) O1s and (b) C1s

The O1s core level spectra of ZnO_R layers are presented in Figure 3.5 (a). The asymmetric O1s core level peaks were deconvoluted using Lorentzian-Gaussian (function pseudo-Voigt) fitting analysis. In the O1s spectra of ZnO_R layers, four peaks belonging to oxygen species were observed. The maximum peak values are 530.1, 531.0 eV, 531.8 and 533 eV. The peaks are ascribed to Me-O bond or to Zn-O in our case [90], oxygen vacancies (Vo) [91][92][93], surface hydroxyl (-OH) groups [94], and surface adsorbed H₂O species [95], respectively. Table 3.1 summarizes the relative amounts of oxygen species, carbon species and water contact angle values of the ZnO_R surfaces.

Table 3.1 Summary of XPS O1s and C1s data obtained from fitting calculations regarding the binding energy values, relative amounts and XPS peak intensities of binding species, and their respective assignments for ZnO_R

Sample	[Vo]/[Me-O]	[OH]/[Me-O]	C=C 285eV	C-O 286.4eV	COOH/C=O 288.9±0.4 eV	N-C-O//C-F _x 293.4±0.5 eV
ZnO _R	0.4	0.5	440	55	130	120

Figure 3.5 (b) represents the C1s core level spectra of ZnO_R layers. The C1s core level spectra of the ZnO_R layers are resolved into four peaks with BE at 285 eV, 286.4 eV, 288.9±0.4 eV and 293.4±0.5 eV, corresponding to the C=C, C-O-C/C-O, COOH/C=O and N-C-O//C-F_x species respectively [96].

Looking at the XPS spectra of the 1Cs core level spectra of ZnO_R it can be concluded, that hydrocarbon species (C=C) are more dominant over the oxygen-containing organics (C-O-C/C-O, COOH/C=O, N-C-O).

Wettability and PL studies provided additional information on the wetting properties of the ZnO_R surface. The average water contact angle values from ZnO_R surface is 5-7.

According to the room temperature PL spectra presented in Figure 7, PL spectra of ZnO_R layer exhibit self-activated emission (SA) band at around 500-550 nm associated with

oxygen vacancy defects [97]. It has been numerously reported, the oxygen vacancy defects possess enhanced adsorption energy and consequently, a high capability to bind the hydroxyl groups. The strong interdependency between the number of oxygen vacancy defects and hydroxyl groups has been clearly demonstrated on electrochemically deposited ZnO nanorods by Gromyko et al [87].

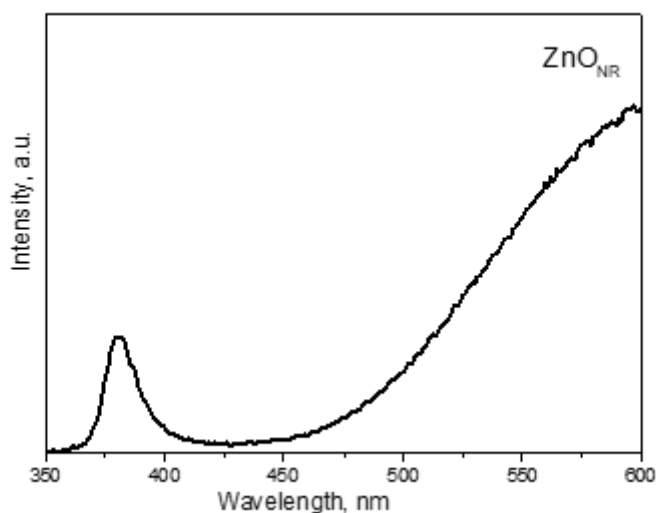


Figure 3.6 RT PL spectra of ZnO_R layers.

3.5 Photocatalytic activity of the ZnO_R photocatalyst

The photocatalytic performance of the ZnO_R layers was evaluated by photodegradation rate of MO, MB, and RhB under UV irradiation. The C/C_0 curves as a function of time were plotted as shown in Figure 3.7 for the three dyes using initial dye concentration of 0.01 mg/L. A linear relationship in the graphs of $\ln(C_0/C)$ vs. illumination time for the photocatalytic degradation of MO, MB and RhB is confirmatory of the pseudo-first-order reaction kinetic model [34]. The apparent first order rate constant, k_{obs} is evaluated from the linear regression of the $\ln(C_0/C)$ vs. time curve presented in Figure (3.8) for the three dyes. The summary of the data obtained from Figure 3.8. along with the calculated correlation coefficient R^2 is presented in Table 3.2. From the table, it is evident that all the correlation coefficients are greater than 0.95, which reveals that the dye's photodegradation conforms with the chosen kinetic model.

Table 3.2 Summary of the data obtained from the photocatalytic study. C/C_0 , k_{obs} and R^2 for ZnO_R layers equalized by same surface area and mass with ZnO_R sample

Sample	C/C_0 , % for 3 h			k_{obs}			R^2		
	MO	MB	RhB	MO	MB	RhB	MO	MB	RhB
ZnO_R	68	55	67	0.006	0.004	0.006	0.99	0.98	0.99

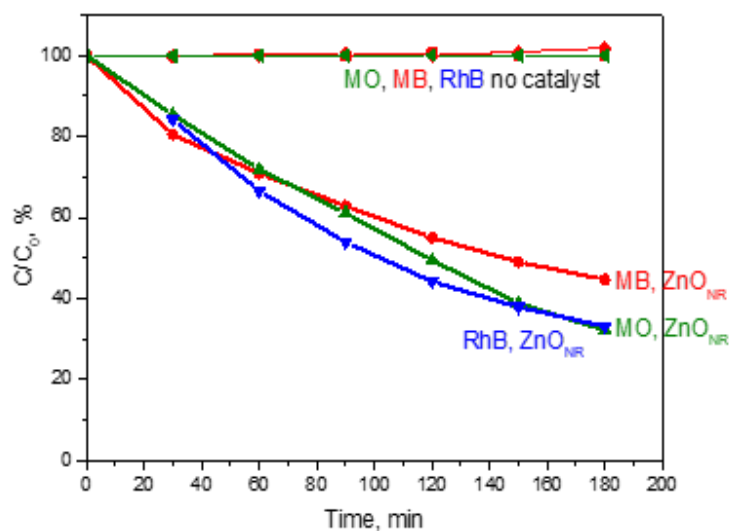


Figure 3.7 Photocatalytic degradation rate C/C_0 vs. time of MO (10 ppm), MB (10 ppm) and RhB (10 ppm) by ZnO_R photocatalyst under UV illumination.

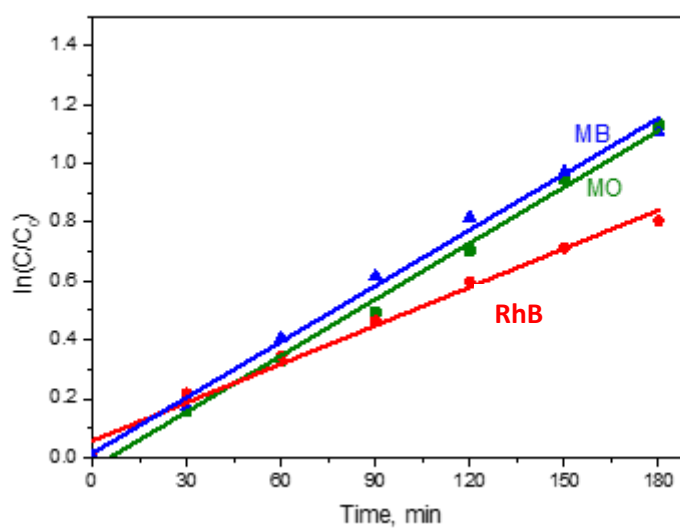


Figure 3.8 Plots of $\ln(C_0/C)$ as a function vs illumination time for the degradation of MO, MB and RhB by the as synthesized ZnO_R photocatalyst.

According to the values of the percentages of MO, MB and RhB discoloration over the time using the same area of the photocatalysts as shown in Figure 3.7., it was observed that the ZnO_R layers photocatalytic efficiency was the same for MO and RhB and lower for MB after 3 h. For instance, ZnO_R samples used in the experiment showed ca. 68 %/3h of degradation efficiency for MO dye, 67 %/3h degradation efficiency for RhB, and a poor degradation of only 55 % for MB molecule. In the absence of the ZnO_R photocatalyst, no reduction was seen in the measured absorbance peak, indicating an absence of pollutant degradation.

3.6 Discussion

The molecular structures of the MO and MB dyes are represented in Table 1.3. MO is an anionic dye having the azo functional group, -N=N- in the middle of the molecule. The mechanism of photodegradation of MO has been studied by several authors. Ke Dai et al. [98] and Bianco-Prevot [99] have reported the two principal mechanisms of MO degradation: hydroxylation and demethylation. K. Dai and major other studies point out the hydroxylation as a dominant mechanism of MO degradation considering that the hydroxyl radicals prefer to attack the electron-rich sites, and that the high surface areas of photocatalyst are usually producing high amount of hydroxyl radicals. The scheme of MO decomposition by hydroxylation mechanism is sketched in Figure 3.9 (a). During hydroxylation, the hydroxyl radical attacks and breaks the C-S, C-N, and N=N bonds of MO. Assuming the hydroxylation as a leading mechanism in our case for MO degradation, this is a possible explanation of better photodegradation response of superhydrophilic ZnO_R surfaces towards MO photocatalyst.

As opposed to MO and RhB dyes, MB dye has a cationic charge and is more hydrophobic due to the presence of highly hydrophobic benzene rings and four hydrophobic methyl (-CH₃) groups. Demethylation reactions with auxochrome group degradation (methyl groups), followed by substitution of the methyl groups with H- atoms and finally, hydroxylation with central aromatic heterocycle ring-opening of MB molecule are considered the primary mechanisms for MB decomposition. The reduction of peak intensity with illumination time corresponds to mineralization and formation of volatile species only.

In the case of Rhodamine B, it is thought that the degradation starts with the attack of active hydroxyl ($\cdot OH$) radicals on its conjugated large π -bond chromophore followed by decarboxylation and denitrification [100]. Further attack by the same radical opens

up the benzene ring thus forming oxalic acid, which eventually mineralizes into CO_2 and H_2O .

Thus a fundamental understanding of the dye degradation mechanisms and studies on photocatalysts surface properties could assist in the design of a highly active photocatalyst for certain dye molecules to be decomposed more efficiently.

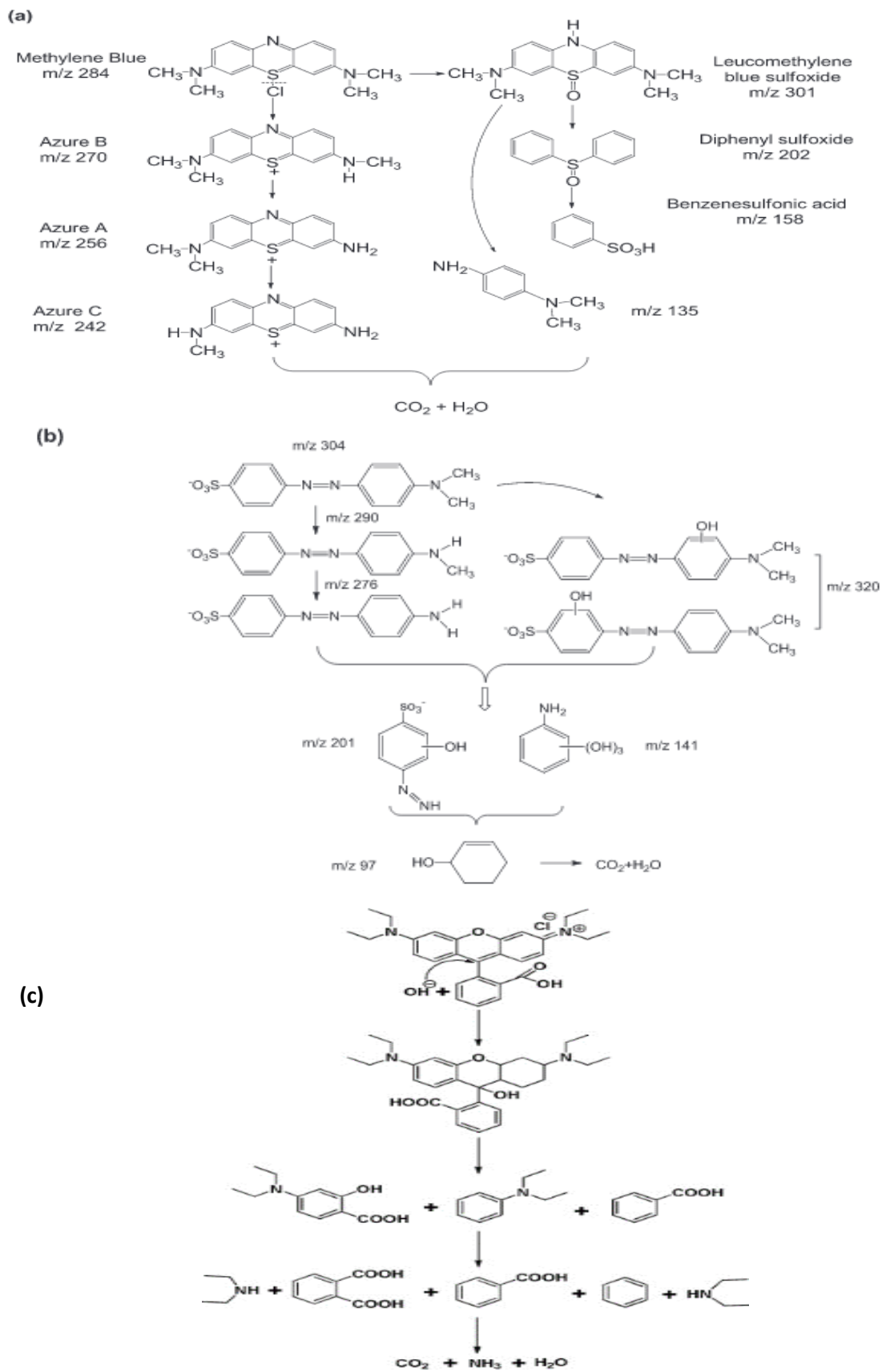


Figure 3.9 Proposed degradation pathway for a) methylene blue (MB), b) methyl orange (MO) and c) rhodamine B (RhB)

4. CONCLUSIONS

1. The SEM and XRD studies reveal that elongated ($L = 1 \mu\text{m}$, $d = 50\text{-}150 \text{ nm}$), highly c-axis oriented ZnO nanorods vertically to the substrate, have been grown by hydrothermal growth method.
2. The main properties of the zinc oxide nanorods were studied. The E_g of the ZnO_R is 3.27 eV, the transmittance is ca. 55% in the wavelength range of 385 nm. The ZnO_R are superhydrophilic, with a water contact angle of 6-7. The PL spectra of ZnO_R layer exhibit self-activated emission (SA) band at around 500-550 nm associated with oxygen vacancy defects. XPS study have shown that oxygen vacancies and hydroxide groups are present on the surface of the ZnO nanorods.
3. The ZnO nanorods are photocatalytically active towards different dyes. The highest photocatalytic activity was achieved on MO and RhB dyes, with decomposition rates of 68% and 67% for 3h, respectively. The MB decomposition rate was lower, with a value of 55% for 3h.
4. A short schematic summary showing possible mechanisms of degradation of different dyes by ZnO_R was presented.

SUMMARY

Zinc oxide nanorod layers were successfully synthesized via a facile and cost-effective hydrothermal method. Synthesis was carried out using precursor solution containing equimolar concentrations of zinc nitrate hexahydrate ($\text{Zn}(\text{NO}_3)_2 \cdot 6\text{H}_2\text{O}$; Sigma-Aldrich, 99.9 %) and hexamethylenetetramine ($\text{CH}_2)_6\text{N}_4$; HMTA; Sigma-Aldrich) 0.1 mol/l. processing temperature and time were 120°C and 2 hours respectively. In order to ensure that the ZnO_R layers were aligned in a vertical orientation to the substrate, seed layers were deposited by spray pyrolysis onto the glass substrate before the commencement of the hydrothermal deposition.

SEM studies reveal agglomerated clumps of c-axes oriented ZnO nanoparticles on the substrate. There is a dense coverage of elongated ZnO rod crystals with average lengths of the crystals ca. 1 μm , and diameters vary from 50 to 150 nm. Vertical orientation of the crystals prevails indicating nanorods grown on nucleation seeds with the (0001) planes parallel to the substrate.

According to XRD pattern of the ZnO_R nanorod layers, high crystallinity is evident with the main reflections at 2θ of 31.77, 34.42, 36.25, 47.54, 56.6° correspond to (100), (002), (101), (102) and (110) planes of hexagonal ZnO.

The total transmittance (TT) and total reflectance spectra of the ZnO_R arrays was measured in the wavelength range between 300 – 2000 nm. The TT plot of ZnO_R reveal a sharp band edge at about 385 nm which correlates to the bandgap value of ZnO. Total reflectance of ZnO_R , was 35 % at 380 nm and gradually decreased to ca. 30% at 550 nm. Such a slump is characteristic of samples containing a fine-grained structure.

XPS spectra reveals four peaks belonging to oxygen species. The peaks maximum values are 530.1, 531.0 eV, 531.8 and 533 eV and correspond to Me-O bond or to Zn-O in our case, oxygen vacancies (V_o) surface hydroxyl (-OH) groups, and surface adsorbed H_2O species respectively.

The presence of oxygen vacancies is confirmed by room temperature PL spectra. The PL spectra of ZnO_R layers exhibit self-activated emission (SA) band at around 500-550 nm associated with oxygen vacancy defect. The oxygen vacancy defects possess enhanced adsorption energy and consequently a high capability to bind the hydroxyl groups.

According to the values of the percentages of MO, MB and RhB discoloration over the time obtained, ZnO_R showed an equivalent photodegradation efficiency for MO and RhB and lower for MB after 3 h. Efficiencies were ca. 68 %/3h for MO dye, 67 %/3h for RhB, and a degradation of only 55 % for the MB dye. In the absence of the ZnO_R photocatalyst, no reduction was seen in the measured absorbance peak, indicating an absence of pollutant degradation.

ACKNOWLEDGEMENTS

I want to express my sincere gratitude and thanks to my supervisor Dr. Tatjana Dedova for her unflinching support during this study. I would also like to thank Dr. Atanas Katerski for his assistance in the various experimental setup, Dr. Mati Danilson for recording the XPS spectra and Dr. Valdek Mikli for helping out with the SEM imaging.

I am indebted to the Department of Materials and Environmental Technology especially, Professors Malle Krunk and Ilona Oja Acik for their feedbacks.

I also acknowledge the Estonian Research Council projects IUT19-4 "Thin films and nanomaterials by wet-chemical methods for next-generation photovoltaics", PRG627 "Antimony chalcogenide thin films for next-generation semi-transparent solar cells applicable in electricity producing windows" and European Regional Development Fund project TK141 "Advanced materials and high-technology devices for sustainable energetics, sensorics and nanoelectronics" for funding.

Finally, I would like to thank my family and friends for their usual support and encouragement

LIST OF FIGURES

Figure 1.1 Overview of dye removal processes [21]	15
Figure 1.2 The photodegradation of an organic molecule by a ZnO photocatalyst [26]	16
Figure 1.3 Effect of calcination temperature on the photocatalytic properties of ZnO [32].....	21
Figure 1.4 Effect of initial dye concentration on the photocatalytic degradation [34]..	22
Figure 1.5 Plots showing the removal percent as a function of MB degradation versus Time (min). (a) in the dark; (b) under UV illumination [34]	22
Figure 1.6 Effect of pH on photocatalytic degradation of MB dye under conditions, pH= 1-10. [37]	24
Figure 1.7 Geometric derivation of Bragg's law: Constructive interference occurs when the delay between waves scattered from adjacent lattice planes given by $a_1 + a_2$ is an integer multiple of the wavelength λ . (that is, when the waves are in alignment) [39]	25
Figure 1.8 The parameters of the electron beam with the greatest impact on the sharpness, resolution and visibility of SEM images are the electron probe size (d_p), electron probe current (i_p) and electron probe convergence angle (α_p). [41]	26
Figure 1.9 Photoelectron and Auger electron emission process [55]	28
Figure 1.10 UV-Vis spectra changes of AR14 (20 ppm) in aqueous ZnO dispersion (ZnO 160 ppm) irradiated with a mercury lamp light at pH neutral, at times: (1) zero, (2) 15 min, (3) 30 min, and (4) 60 min where ppm = mg/kg \approx mg/L = g/m ³ . [51]..	29
Figure 1.11 Crystal structure of $2 \times 2 \times 2$ supercell wurtzite ZnO [54].....	30
Figure 1.12 Ball and stick representation of ZnO crystal structures: (a) cubic rocksalt (B1), (b) cubic zinblende (B3) and (c) hexagonal wurtzite (B4) [56].....	31
Figure 1.13 ZnO _R morphological model showing the top surface of O-(0001 ⁻) terminations and the bottom surface of Zn-(0001) terminations.	32
Figure 1.14 Schematic diagram of the preparation of ZnO nanomaterials by hydrothermal synthesis route [65].....	34
Figure 1.15 SEM images showing morphology of ZnO crystals prepared at varying pH = (a) 9, (b) 10, (c) 11, and (d) 12 [68].....	36
Figure 1.16 SEM images showing the influence of time on the hydrothermal growth of ZnO crystals. Using Zn(NO ₃) ₂ ·0.04 mol/L: HMTA-0.025 M at 75°C: a) 15 min, (b) 30 min and (c) 60 min [69]	37
Figure 1.17 SEM images of ZnO powder hydrothermally prepared at (a) 100°C, (b) 150°C, and (c) 200°C for 2 h. [68]	38
Figure 1.18 SEM images showing ZnO nanostructures synthesized at different origin of seed layer: (a) on clear glass, (b) on MS seeds, (c) on ED seeds, (d) on AD seeds. Other parameters were: 0.1 M Zn(NO ₃) ₂ + HMTA equimolar solution, t = 3 h, T = 90 °C [62]	39
Figure 2.1 Image of a spray pyrolysis equipment – courtesy of thin film laboratory technology - Taltech	43
Figure 2.2 Steel autoclave reactor Berghof BR-100 from the Thin film technology laboratory – Taltech.....	44
Figure 3.1 SEM images from the surface (a) and cross-section (b) of a ZnO-NR	46
Figure 3.2 XRD pattern of hydrothermally grown ZnOR showing a prominent (002) peak	47
Figure 3.3 Total transmittance (TT) and total reflectance (TR) plots of ZnO _R layers ...	48
Figure 3.4 $(\alpha h\nu)^2$ vs. energy plot - Bang gap (E_g) determination for ZnO layers from Tauc's plot.	49
Figure 3.5 ZnOR XPS spectra in the binding energy region of (a) O1S and (b) C1S ...	50
Figure 3.6 RT PL spectra of ZnO _R layers.....	51

Figure 3.7 Photocatalytic degradation rate C/C_0 vs. time of MO (10 ppm), MB (10 ppm) and RhB (10 ppm) by ZnO_R photocatalyst under UV illumination.....	52
Figure 3.8 Plots of $\ln(C_0/C)$ as a function vs illumination time for the degradation of MO, MB and RhB by the as synthesized ZnO_R photocatalyst.	52
Figure 3.9 Proposed degradation pathway for a) methylene blue (MB), b) methyl orange (MO) and c) rhodamine B (RhB).....	55

LIST OF TABLES

Table 1.1: Classification of water pollutants [28]	12
Table 1.2: Structure and properties of dye molecules	14
Table 1.3 Number of times ZnO was mentioned in literature (1980 – 2020) in connection with the degradation of methyl orange, methylene blue, rhodamine-B [7]	15
Table 1.4 Properties of wurtzite ZnO [54]	30
Table 1.5 Photocatalytic activity comparison of various ZnO morphologies fabricated by hydrothermal method	40
Table 3.1 Summary of XPS O1s and C1s data obtained from fitting calculations regarding the binding energy values, relative amounts and XPS peak intensities of binding species, and their respective assignments for ZnO _R	50
Table 3.2 Summary of the data obtained from photocatalytic study. C/C0, Kobs and R2 for ZnOR layers equalized by same surface area and mass with ZnO _R sample	52

REFERENCES

- [1] L. Pereira and M. Alves, "Dyes-environmental impact and remediation," in *Environmental Protection Strategies for Sustainable Development*, Springer Netherlands, 2012, pp. 111–162.
- [2] H. A. Abbas, R. A. Nasr, A. Khalaf, A. Al Bawab, and T. S. Jamil, "Photocatalytic degradation of methylene blue dye by fluorite type Fe₂Zr₂-xWxO₇ system under visible light irradiation," *Ecotoxicol. Environ. Saf.*, vol. 196, p. 110518, Jun. 2020.
- [3] R. Kant, "Textile dyeing industry an environmental hazard," *Nat. Sci.*, vol. 04, no. 01, pp. 22–26, Dec. 2012.
- [4] P. Cañizares *et al.*, "Electrochemical oxidation of azoic dyes with conductive-diamond anodes," *Ind. Eng. Chem. Res.*, vol. 45, no. 10, pp. 3468–3473, May 2006.
- [5] A. Santos, P. Yustos, S. Rodríguez, F. Garcia-Ochoa, and M. de Gracia, "Decolorization of Textile Dyes by Wet Oxidation Using Activated Carbon as Catalyst," *Ind. Eng. Chem. Res.*, vol. 46, no. 8, pp. 2423–2427, Apr. 2007.
- [6] Y. Wang, L. Gai, W. Ma, H. Jiang, X. Peng, and L. Zhao, "Ultrasound-Assisted Catalytic Degradation of Methyl Orange with Fe₃O₄/Polyaniline in Near Neutral Solution," *Ind. Eng. Chem. Res.*, vol. 54, no. 8, pp. 2279–2289, Mar. 2015.
- [7] H. Li, Y. Gong, Q. Huang, and H. Zhang, "Degradation of Orange II by UV-Assisted Advanced Fenton Process: Response Surface Approach, Degradation Pathway, and Biodegradability," *Ind. Eng. Chem. Res.*, vol. 52, no. 44, pp. 15560–15567, Nov. 2013.
- [8] U. I. Gaya, *Heterogeneous photocatalysis using inorganic semiconductor solids*. 2014.
- [9] "Web of Science [v.5.34] - Web of Science Core Collection Full Record." [Online]. Available: http://apps.webofknowledge.com/full_record.do?product=WOS&search_mode=GeneralSearch&qid=28&SID=E4YfeVzYVysPXWKBW9r&page=1&doc=1. [Accessed: 03-Feb-2020].
- [10] T. Wang *et al.*, "Novel Bi₂WO₆ loaded N-biochar composites with enhanced photocatalytic degradation of rhodamine B and Cr(VI)," *J. Hazard. Mater.*, vol. 389, p. 121827, May 2020.
- [11] M. Kummu *et al.*, "The world's road to water scarcity: Shortage and stress in the 20th century and pathways towards sustainability," *Sci. Rep.*, vol. 6, no. 1, pp. 1–16, Dec. 2016.
- [12] "Industrial Waste — Safe Drinking Water Foundation." [Online]. Available: <https://www.safewater.org/fact-sheets-1/2017/1/23/industrial-waste>. [Accessed: 03-Feb-2020].
- [13] M. L. McKinney, R. M. Schoch, and L. Yonavjak, *Environmental science : systems and solutions*. Jones and Bartlett Publishers, 2007.
- [14] H. Qadri, R. Ahmad, B. Mohammad, A. Mehmood, and G. Hamid, *Fresh Water Pollution Dynamics and Remediation*. 2020.
- [15] P. Nidheesh, M. Zhou, and M. A. Oturan, "An overview on the removal of synthetic dyes from water by electrochemical advanced oxidation processes."

- [16] L. Laysandra *et al.*, "Adsorption and photocatalytic performance of bentonite-titanium dioxide composites for methylene blue and rhodamine B decoloration," *Heliyon*, vol. 3, no. 12, p. e00488, Dec. 2017.
- [17] S. S. Muthu, *Textile Science and Clothing Technology*. 2018.
- [18] G. Byzinski, A. P. Pereira, D. P. Volanti, C. Ribeiro, and E. Longo, "High-performance ultraviolet-visible driven ZnO morphologies photocatalyst obtained by microwave-assisted hydrothermal method," *J. Photochem. Photobiol. A Chem.*, vol. 353, pp. 358–367, 2018.
- [19] K. Byrappa, A. K. Subramani, S. Ananda, K. M. Lokanatha Rai, R. Dinesh, and M. Yoshimura, "Photocatalytic degradation of rhodamine B dye using hydrothermally synthesized ZnO," *Bull. Mater. Sci.*, vol. 29, no. 5, pp. 433–438, 2006.
- [20] A. Gil, L. A. Galeano, and M. A. Vincente, *Applications of Advanced Oxidation Processes (AOPs) in Drinking Water Treatment*. 2018.
- [21] M. Cheng *et al.*, "Hydroxyl radicals based advanced oxidation processes (AOPs) for remediation of soils contaminated with organic compounds: A review," *Chemical Engineering Journal*, vol. 284. Elsevier, pp. 582–598, 15-Jan-2016.
- [22] P. Jongnavakit, P. Amornpitoksuk, S. Suwanboon, and N. Ndiege, "Preparation and photocatalytic activity of Cu-doped ZnO thin films prepared by the sol-gel method," *Appl. Surf. Sci.*, vol. 258, no. 20, pp. 8192–8198, 2012.
- [23] S. K. Kansal, M. Singh, and D. Sud, "Studies on photodegradation of two commercial dyes in aqueous phase using different photocatalysts," *J. Hazard. Mater.*, vol. 141, no. 3, pp. 581–590, Mar. 2007.
- [24] J. H. Sun, S. Y. Dong, Y. K. Wang, and S. P. Sun, "Preparation and photocatalytic property of a novel dumbbell-shaped ZnO microcrystal photocatalyst," *J. Hazard. Mater.*, vol. 172, no. 2–3, pp. 1520–1526, 2009.
- [25] K. Kakaei, M. D. Esrafil, and A. Ehsani, "Introduction to Catalysis," in *Interface Science and Technology*, vol. 27, Elsevier B.V., 2019, pp. 1–21.
- [26] S. Malato, P. Fernández-Ibáñez, M. I. Maldonado, J. Blanco, and W. Gernjak, "Decontamination and disinfection of water by solar photocatalysis: Recent overview and trends," *Catalysis Today*, vol. 147, no. 1. pp. 1–59, 15-Sep-2009.
- [27] H. Gerischer and A. Heller, "The role of oxygen in photooxidation of organic molecules on semiconductor particles," *J. Phys. Chem.*, vol. 95, no. 13, pp. 5261–5267, 1991.
- [28] J. M. Herrmann, "Heterogeneous photocatalysis: Fundamentals and applications to the removal of various types of aqueous pollutants," *Catal. Today*, vol. 53, no. 1, pp. 115–129, Oct. 1999.
- [29] K. M. Lee, C. W. Lai, K. S. Ngai, and J. C. Juan, "Recent developments of zinc oxide based photocatalyst in water treatment technology: A review," *Water Research*, vol. 88. Elsevier Ltd, pp. 428–448, 01-Jan-2016.
- [30] K. H. Wang, Y. H. Hsieh, C. H. Wu, and C. Y. Chang, "The pH and anion effects on the heterogeneous photocatalytic degradation of o-methylbenzoic acid in TiO₂ aqueous suspension," *Chemosphere*, 2000.
- [31] W. Baran, A. Makowski, and W. Wardas, "The effect of UV radiation absorption of cationic and anionic dye solutions on their photocatalytic degradation in the presence TiO₂," *Dye. Pigment.*, 2008.
- [32] X. Chen, Z. Wu, D. Liu, and Z. Gao, "Preparation of ZnO Photocatalyst for the

- Efficient and Rapid Photocatalytic Degradation of Azo Dyes," *Nanoscale Res. Lett.*, vol. 12, no. 1, Dec. 2017.
- [33] S. Selvarajan, P. Malathy, A. Suganthi, and M. Rajarajan, "Fabrication of mesoporous BaTiO₃/SnO₂ nanorods with highly enhanced photocatalytic degradation of organic pollutants," *J. Ind. Eng. Chem.*, vol. 53, pp. 201–212, Sep. 2017.
- [34] S. M. Saleh, "Metal Oxide Nanomaterials as Photo-Catalyst for Dye Degradation."
- [35] A. Akyol and M. Bayramoğlu, "Photocatalytic degradation of Remazol Red F3B using ZnO catalyst," *J. Hazard. Mater.*, 2005.
- [36] A. P. Davis and C. P. Huang, "Removal of phenols from water by a photocatalytic oxidation process," *Water Sci. Technol.*, vol. 21, no. 6-7-7 pt 2, pp. 455–464, Jun. 1989.
- [37] K. A. Isai and V. S. Shrivastava, "Photocatalytic degradation of methylene blue using ZnO and 2% Fe-ZnO semiconductor nanomaterials synthesized by sol-gel method: A comparative study," *J. Water Environ. Nanotechnol*, vol. 4, no. 3, pp. 251–262, 2019.
- [38] M. Sardela, *Practical materials characterization*. 2014.
- [39] H. Stanjek and W. Häusler, "Basics of X-ray diffraction," *Hyperfine Interact.*, 2004.
- [40] S. K. Sharma, D. S. Verma, L. U. Khan, S. Kumar, and S. B. Khan, *Handbook of Materials Characterization*. 2018.
- [41] D. A. Skoog, D. M. West, F. J. Holler, and S. R. Crouch, "Skoog and West's Fundamentals of Analytical Chemistry," in *Skoog and West's Fundamentals of Analytical Chemistry*, 2014.
- [42] C. S. S. R. Kumar, *UV-VIS and photoluminescence spectroscopy for nanomaterials characterization*. 2013.
- [43] L. He, Z. Tong, Z. Wang, M. Chen, N. Huang, and W. Zhang, "Effects of calcination temperature and heating rate on the photocatalytic properties of ZnO prepared by pyrolysis," *J. Colloid Interface Sci.*, vol. 509, pp. 448–456, 2018.
- [44] Y. Y. Wang, G. Q. Zhou, L. Zhang, and T. Q. Liu, "Synthesis and photocatalytic characterization of porous Cu-doped ZnO nanorods," *Wuli Huaxue Xuebao/ Acta Phys. - Chim. Sin.*, vol. 32, no. 11, pp. 2785–2793, 2016.
- [45] U. Diebold and T. E. Madey, "TiO₂ by XPS," *Surf. Sci. Spectra*, 1996.
- [46] S. Verdier, L. El Ouatani, R. Dedryvère, F. Bonhomme, P. Biensan, and D. Gonbeau, "XPS study on Al₂O₃- and AlPO₄-coated LiCoO₂ cathode material for high-capacity Li ion batteries," *J. Electrochem. Soc.*, 2007.
- [47] Y. Lu, Y. Lin, D. Wang, L. Wang, T. Xie, and T. Jiang, "A high performance cobalt-doped ZnO visible light photocatalyst and its photogenerated charge transfer properties," *Nano Res.*, vol. 4, no. 11, pp. 1144–1152, 2011.
- [48] H. Ma *et al.*, "Synthesis, characterization and photocatalytic activity of Cu-doped Zn/ZnO photocatalyst with carbon modification," *J. Mater. Chem.*, vol. 22, no. 45, pp. 23780–23788, 2012.
- [49] R. Raji, K. S. Sibi, and K. G. Gopchandran, "ZnO:Ag nanorods as efficient photocatalysts: Sunlight driven photocatalytic degradation of sulforhodamine B,"

- Appl. Surf. Sci.*, vol. 427, pp. 863–875, 2018.
- [50] Y. H. Chiu, T. F. M. Chang, C. Y. Chen, M. Sone, and Y. J. Hsu, "Mechanistic insights into photodegradation of organic dyes using heterostructure photocatalysts," *Catalysts*, vol. 9, no. 5, 2019.
- [51] N. Daneshvar, D. Salari, and A. R. Khataee, "Photocatalytic degradation of azo dye acid red 14 in water on ZnO as an alternative catalyst to TiO₂," *J. Photochem. Photobiol. A Chem.*, vol. 162, no. 2–3, pp. 317–322, 2004.
- [52] C. Jagadish and S. Pearton, *Zinc Oxide Bulk, Thin Films and Nanostructures*. Elsevier Ltd, 2006.
- [53] C. F. Klingshirn, B. K. Meyer, A. Waag, A. Hoffmann, and J. Geurts, *Zinc Oxide : From FUndamental Properties Towards Novel Applications, Springer Series in Materials Science*. 2013.
- [54] S. Wang, Z. Jin, X. Huang, S. Peng, D. Zhang, and J. Shi, "Sol-gel synthesized ZnO for optoelectronics applications: a characterization review Related content," 2016.
- [55] Z. Fan and J. G. Lu, "Zinc Oxide Nanostructures: Synthesis and Properties."
- [56] C. F. Klingshirn, B. K. Meyer, A. Waag, A. Hoffmann, and J. Geurts, *Zinc Oxide - From Fundamental Properties Towards Novel Applications*, no. 1. Springer, 2010.
- [57] S. P. Meshram, P. V. Adhyapak, D. P. Amalnerkar, and I. S. Mulla, "Cu doped ZnO microballs as effective sunlight driven photocatalyst," *Ceram. Int.*, vol. 42, no. 6, pp. 7482–7489, 2016.
- [58] B. M. Rajbongshi and S. K. Samdarshi, "ZnO and Co-ZnO nanorods - Complementary role of oxygen vacancy in photocatalytic activity of under UV and visible radiation flux," *Mater. Sci. Eng. B Solid-State Mater. Adv. Technol.*, vol. 182, no. 1, pp. 21–28, 2014.
- [59] C. Wu, L. Shen, H. Yu, Y. C. Zhang, and Q. Huang, "Solvothermal synthesis of Cu-doped ZnO nanowires with visible light-driven photocatalytic activity," *Mater. Lett.*, vol. 74, pp. 236–238, 2012.
- [60] N. Kumaresan, K. Ramamurthi, R. Ramesh Babu, K. Sethuraman, and S. Moorthy Babu, "Hydrothermally grown ZnO nanoparticles for effective photocatalytic activity," *Appl. Surf. Sci.*, vol. 418, pp. 138–146, 2017.
- [61] S. Kuriakose, B. Satpati, and S. Mohapatra, "Enhanced photocatalytic activity of Co doped ZnO nanodisks and nanorods prepared by a facile wet chemical method," *Phys. Chem. Chem. Phys.*, vol. 16, no. 25, pp. 12741–12749, 2014.
- [62] V. Gerbreder *et al.*, "Hydrothermal synthesis of ZnO nanostructures with controllable morphology change," *CrystEngComm*, vol. 22, no. 8, pp. 1346–1358, Feb. 2020.
- [63] N. H. Nickel and E. Terukov, *Zinc oxide - a material for micro- and optoelectronic applications*. Springer, 2005.
- [64] R. S. Sabry, M. A. Abid, B. Muhsen, and W. J. Aziz, "Hydrothermal controllable synthesis to convert ZnO hexagonal nanotubes to hexagonal nanorods and their photocatalytic application," *J. Mater. Sci. Mater. Electron.*, vol. 27, no. 11, pp. 11176–11181, Nov. 2016.
- [65] M. Makkar, • H S Bhatti, and K. Singh, "Effect of reaction conditions on the morphology and optical properties of ZnO nanocrystals."

- [66] A. P. Kerasidou *et al.*, "Growth of ZnO nanowires on seeding layers deposited by ALD: The influence of process parameters," *Microelectron. Eng.*, vol. 217, p. 111091, Sep. 2019.
- [67] W. Suchanek, "Systematic Study of Hydrothermal Synthesis of Zinc Oxide (ZnO) Nanosized Powders with Superior UV Absorption," *Sawyerllc.Com*, pp. 1–31, 2008.
- [68] C. H. Lu and C. H. Yeh, "Influence of hydrothermal conditions on the morphology and particle size of zinc oxide powder," *Ceram. Int.*, vol. 26, no. 4, pp. 351–357, May 2000.
- [69] D. Polsongkram *et al.*, "Effect of synthesis conditions on the growth of ZnO nanorods via hydrothermal method," *Phys. B Condens. Matter*, vol. 403, no. 19–20, pp. 3713–3717, Oct. 2008.
- [70] E. M. Wong, J. E. Bonevich, and P. C. Searson, "Growth kinetics of nanocrystalline ZnO particles from colloidal suspensions," *J. Phys. Chem. B*, vol. 102, no. 40, pp. 7770–7775, Oct. 1998.
- [71] D. Cao, S. Gong, X. Shu, D. Zhu, and S. Liang, "Preparation of ZnO Nanoparticles with High Dispersibility Based on Oriented Attachment (OA) Process," *Nanoscale Res. Lett.*, vol. 14, no. 1, p. 210, Dec. 2019.
- [72] M. A. Mahmood, S. Jan, I. A. Shah, and I. Khan, "Review Article Growth Parameters for Films of Hydrothermally Synthesized One-Dimensional Nanocrystals of Zinc Oxide," 2016.
- [73] H. T. Kim, S. Y. Lee, and Y. S. Sohn, "Formation mechanism and properties of nanorod-structured ZnO films prepared by pyrolysis of Zn acetate films," *Vacuum*, vol. 155, pp. 403–407, Sep. 2018.
- [74] P. Gowthaman, M. Saroja, M. Venkatachalam, J. Deenathayalan, and T. S. Senthil, "Photocatalytic degradation of methylene blue dye using hydrothermally synthesized ZnO nanorods," *Optoelectron. Adv. Mater. Rapid Commun.*, vol. 5, no. 12, pp. 1307–1311, 2011.
- [75] M. Kardeş and K. Öztürk, "Photocatalyst ZnO nanorod arrays on glass substrates: the critical role of seed layer in nanorod alignment and photocatalytic efficiencies," *Chem. Eng. Commun.*, pp. 1–14, Sep. 2019.
- [76] E. Karaköse and H. Çolak, "Structural and optical properties of ZnO nanorods prepared by spray pyrolysis method," *Energy*, vol. 140, pp. 92–97, Dec. 2017.
- [77] H. wa Yu, J. Wang, C. juan Xia, X. an Yan, and P. fei Cheng, "Template-free hydrothermal synthesis of Flower-like hierarchical zinc oxide nanostructures," *Optik (Stuttg.)*, vol. 168, pp. 778–783, Sep. 2018.
- [78] "Chinese Physics B Synthesis of Pr-doped ZnO nanoparticles: Their structural, optical, and photocatalytic properties *," 2018.
- [79] Bhawna, B. P. Majee, V. Choudhary, R. Prakash, and A. K. Mishra, "Hydrothermally grown ZnO nanoparticles for photodegradation of textile dye," in *AIP Conference Proceedings*, 2019, vol. 2100, no. 1, p. 020073.
- [80] G. Poongodi, R. Mohan Kumar, and R. Jayavel, "Influence of S doping on structural, optical and visible light photocatalytic activity of ZnO thin films," *Ceram. Int.*, vol. 40, no. 9 PART B, pp. 14733–14740, 2014.
- [81] S. Yi, J. Cui, S. Li, L. Zhang, D. Wang, and Y. Lin, "Enhanced visible-light photocatalytic activity of Fe/ZnO for rhodamineB degradation and its photogenerated charge transfer properties," *Appl. Surf. Sci.*, vol. 319, no. 1, pp.

230–236, 2014.

- [82] N. Chauhan, V. Singh, S. Kumar, M. Kumari, and K. Sirohi, "Synthesis of sulphur & indium co-doped mesoporous zinc oxide nanoparticles via hydrothermal method to study their photocatalytic activity," *Optik (Stuttg)*, vol. 185, pp. 838–846, May 2019.
- [83] S. M. Saleh, "ZnO nanospheres based simple hydrothermal route for photocatalytic degradation of azo dye," *Spectrochim. Acta - Part A Mol. Biomol. Spectrosc.*, vol. 211, pp. 141–147, Mar. 2019.
- [84] K. Santhi, M. Navaneethan, S. Harish, S. Ponnusamy, and C. Muthamizhchelvan, "Synthesis and characterization of TiO₂ nanorods by hydrothermal method with different pH conditions and their photocatalytic activity," *Appl. Surf. Sci.*, vol. 500, Jan. 2020.
- [85] V. Mata, A. Maldonado, and M. de la Luz Olvera, "Deposition of ZnO thin films by ultrasonic spray pyrolysis technique. Effect of the milling speed and time and its application in photocatalysis," *Mater. Sci. Semicond. Process.*, vol. 75, pp. 288–295, Mar. 2018.
- [86] T. Dedova *et al.*, "Influence of solution composition on sprayed ZnO nanorods properties and formation process: Thermoanalytical study of the precursors," *Ceram. Int.*, vol. 45, no. 2, pp. 2887–2892, Feb. 2019.
- [87] I. Gromyko, M. Krunks, T. Dedova, A. Katerski, D. Klauson, and I. Oja Acik, "Surface properties of sprayed and electrodeposited ZnO rod layers," *Appl. Surf. Sci.*, vol. 405, pp. 521–528, May 2017.
- [88] Y. Hu, L. Song, Y. Chen, and W. Huang, "Two-Terminal Perovskites Tandem Solar Cells: Recent Advances and Perspectives," *Sol. RRL*, vol. 3, no. 7, p. 1900080, Jul. 2019.
- [89] S. Baruah, M. Jaisai, R. Imani, M. M. Nazhad, and J. Dutta, "Photocatalytic paper using zinc oxide nanorods," *Sci. Technol. Adv. Mater.*, vol. 11, no. 5, 2010.
- [90] D. Pradhan and K. T. Leung, "Vertical growth of two-dimensional zinc oxide nanostructures on ITO-coated glass: Effects of deposition temperature and deposition time," *J. Phys. Chem. C*, vol. 112, no. 5, pp. 1357–1364, Feb. 2008.
- [91] J. H. Zheng, Q. Jiang, and J. S. Lian, "Synthesis and optical properties of flower-like ZnO nanorods by thermal evaporation method," *Appl. Surf. Sci.*, vol. 257, no. 11, pp. 5083–5087, Mar. 2011.
- [92] C. Mao *et al.*, "Effect of B doping on optical, electrical properties and defects of ZnO films," *J. Alloys Compd.*, vol. 676, pp. 135–141, Aug. 2016.
- [93] A. Sahai and N. Goswami, "Probing the dominance of interstitial oxygen defects in ZnO nanoparticles through structural and optical characterizations," *Ceram. Int.*, vol. 40, no. 9 PART B, pp. 14569–14578, Nov. 2014.
- [94] E. De La Rosa *et al.*, "Controlling the growth and luminescence properties of well-faceted ZnO nanorods," *J. Phys. Chem. C*, vol. 111, no. 24, pp. 8489–8495, Jun. 2007.
- [95] L. Grzadziel and M. Krzywiecki, "Ambience-related adsorbates on CuPc surface - Photoemission and thermal desorption spectroscopy studies for control of organic electronics degradation processes," *Synth. Met.*, vol. 210, pp. 141–147, Dec. 2015.
- [96] P. Liu, L. Cao, W. Zhao, Y. Xia, W. Huang, and Z. Li, "Insights into the

- superhydrophobicity of metallic surfaces prepared by electrodeposition involving spontaneous adsorption of airborne hydrocarbons," *Appl. Surf. Sci.*, vol. 324, pp. 576–583, Jan. 2015.
- [97] S. K. Chaudhuri, M. Ghosh, D. Das, and A. K. Raychaudhuri, "Probing defects in chemically synthesized ZnO nanostructures by positron annihilation and photoluminescence spectroscopy," *J. Appl. Phys.*, vol. 108, no. 6, p. 064319, Sep. 2010.
- [98] K. Dai, H. Chen, T. Peng, D. Ke, and H. Yi, "Photocatalytic degradation of methyl orange in aqueous suspension of mesoporous titania nanoparticles," 2007.
- [99] A. Bianco Prevot *et al.*, "Analytical control of photocatalytic treatments: Degradation of a sulfonated azo dye," *Anal. Bioanal. Chem.*, vol. 378, no. 1, pp. 214–220, Jan. 2004.
- [100] N. Guo, H. Liu, Y. Fu, and J. Hu, "Preparation of Fe₂O₃ nanoparticles doped with In₂O₃ and photocatalytic degradation property for rhodamine B," *Optik (Stuttg.)*, vol. 201, p. 163537, Jan. 2020.